A decadal satellite record of gravity wave activity in the lower stratosphere to study polar stratospheric cloud formation

Lars Hoffmann[1], Reinhold Spang[2], Andrew Orr[3], M. Joan Alexander[4], Laura A. Holt[4], and Olaf Stein[1]

[1]Jülich Supercomputing Centre, Forschungszentrum Jülich, Jülich, Germany
[2]Institut für Energie- und Klimaforschung, Forschungszentrum Jülich, Jülich, Germany
[3]British Antarctic Survey, NERC, Cambridge, UK
[4]NorthWest Research Associates, Inc., CoRA Office, Boulder, CO, USA

Correspondence to: L. Hoffmann (l.hoffmann@fz-juelich.de)

Abstract. Atmospheric gravity waves yield substantial small-scale temperature fluctuations that can trigger the formation of polar stratospheric clouds (PSCs). This paper introduces a new satellite record of gravity wave activity in the polar lower stratosphere to investigate this process. The record comprises observations of the Atmospheric InfraRed Sounder (AIRS) aboard NASA's Aqua satellite during January 2003 to December 2012. Gravity wave activity is measured in terms of detrended and noise-corrected $15\,\mu$m brightness temperature variances, which are calculated from AIRS channels that are most sensitive to temperature fluctuations at about $17-32\,$km altitude. The analysis of temporal patterns in the data set revealed a strong seasonal cycle in wave activity with wintertime maxima at mid and high latitudes. The analysis of spatial patterns indicated that orography as well as jet and storm sources are the main cause of the observed waves. Wave activity is closely correlated with $30\,$hPa zonal winds, which is attributed to the AIRS observational filter. We used the new data set to evaluate explicitly resolved temperature fluctuations due to gravity waves in the European Centre for Medium-Range Weather Forecast (ECMWF) operational analysis. It was found that the analysis reproduces orographic and non-orographic wave patterns in the right places, but that wave amplitudes are typically underestimated by a factor of $2-3$. Furthermore, in a first survey of joint AIRS and Michelson Interferometer for Passive Atmospheric Sounding (MIPAS) satellite observations nearly 50 gravity wave-induced PSC formation events were identified. The survey shows that the new AIRS data set can help to better identify such events and more generally highlights the importance of the process for polar ozone chemistry.

1 Introduction

Polar stratospheric clouds (PSCs) play a key role in ozone chemistry in the polar lower stratosphere. The particles provide the surface area for heterogeneous reactions that catalyze the conversion of chlorine from reservoir gases like $ClONO_2$ and HCl into active chlorine radicals, which accelerate ozone loss in the polar lower stratosphere in late winter and spring (Solomon et al., 1986; Solomon, 1999). Furthermore, the sedimentation of large HNO_3-containing cloud particles leads to denitrification of the stratosphere, which in turn decreases NO_2 concentrations, increases $ClO/ClONO_2$ ratios, and accelerates chlorine-catalyzed ozone loss (Toon et al., 1986). PSC particles are typically classified into three different types (Poole and McCormick, 1988; Browell et al., 1990). This includes metastable hydrates of HNO_3 such as nitric acid trihydrate (NAT) (Hanson and

Mauersberger, 1988; Worsnop et al., 1993), supercooled ternary solution (STS) droplets of $H_2SO_4/HNO_3/H_2O$ (Zhang et al., 1993; Carslaw et al., 1994), and water ice (Steele et al., 1983). Thermodynamic analyses indicate that NAT and STS can exist at temperatures well above the frost point of ice, with $T_{ice} < T_{STS} < T_{NAT}$. Typical PSC formation and existence temperatures at 20 km altitude are $T_{ice} = 188$ K, $T_{STS} = 191$ K, and $T_{NAT} = 195$ K (Pawson et al., 1995). However, actual values vary with atmospheric composition and altitude.

Atmospheric gravity waves are an important driver of middle atmosphere dynamics and have a substantial impact on weather and climate. They transport energy and momentum from lower to upper altitudes, contribute to turbulence and mixing, and influence the mean circulation and thermal structure of the middle atmosphere (Lindzen, 1981; Holton, 1982). Gravity waves are triggered by a variety of sources. The most prominent sources are orography (Smith, 1985; Durran and Klemp, 1987; Nastrom and Fritts, 1992) and convection (Pfister et al., 1986; Tsuda et al., 1994; Alexander and Pfister, 1995). Other sources include adjustment of unbalanced flows near jet streams and frontal systems (Fritts and Alexander, 2003; Wu and Zhang, 2004). Here we are interested in gravity waves because they can provide significant local temperature fluctuations that can trigger the formation of PSCs, even if synoptic-scale temperatures are above formation thresholds. Case studies of mountain waves induced by the Scandinavian mountains showed that the waves can cause localized cooling of up to $10 - 15$ K (Carslaw et al., 1998b; Dörnbrack et al., 1999, 2002). The Antarctic Peninsula is another well-known hotspot for the formation of PSCs from mountain waves in the southern hemisphere (Wu and Jiang, 2002; Shibata et al., 2003; Höpfner et al., 2006b; Baumgaertner and McDonald, 2007; Eckermann et al., 2009; Orr et al., 2015). In the Antarctic polar stratosphere wave-induced PSC formation is particularly important in fall or spring, whereas synoptic-scale temperatures in winter are usually well below the PSC formation threshold (Campbell and Sassen, 2008; McDonald et al., 2009; Noel and Pitts, 2012). The Arctic stratospheric vortex is generally warmer and more disturbed due to planetary wave activity, making gravity waves possibly an even more important source of PSCs in the northern hemisphere (Alexander et al., 2013). Although most case studies focus on gravity waves from orographic sources, Hitchman et al. (2003) and Shibata et al. (2003) showed that non-orographic gravity waves can also trigger PSC formation.

Previous studies on PSC formation used mesoscale model output (Höpfner et al., 2006a; Noel and Pitts, 2012; Orr et al., 2015) or global positioning system radio occultation observations (Kohma and Sato, 2011; Alexander et al., 2011, 2013) as a source of information on gravity waves. The use of Atmospheric InfraRed Sounder (AIRS) observations for that purpose was first explored by Eckermann et al. (2009) and Lambert et al. (2012). In this paper we present a new AIRS data set of gravity wave activity in the polar lower stratosphere that can be used to study the impact of gravity wave-induced temperature fluctuations on PSC formation in more detail. The data set is based on a ten-year record (January 2003 to December 2012) of observations and includes more than 5.3×10^9 infrared radiance spectra measured by AIRS at mid and high latitudes during that time. As a measure of gravity wave activity the new data set provides detrended and noise-corrected $15\,\mu$m brightness temperature variances on a $4° \times 2°$ horizontal grid on a daily basis. The AIRS channels selected for the data product provide most sensitivity in the lower and mid stratosphere (about $17 - 32$ km), i. e., in the altitude range that is most relevant for PSC formation. Here we used the new AIRS data set to identify local hotspots and sources of gravity wave activity, to characterize

its seasonal cycle at northern and southern mid and high latitudes, and to analyze correlations with stratospheric background winds.

We exploited the new AIRS data set in two applications. Various studies demonstrated that AIRS measurements are particularly suited to validate high-resolution gravity wave simulations. Some studies focused on the validation of convective waves (Kim et al., 2009; Grimsdell et al., 2010; Stephan and Alexander, 2015; Wu et al., 2015), but case studies for mountain waves have also been shown (Orr et al., 2015). The validation of explicitly resolved temperature fluctuations in high-resolution meteorological analyses is of particular interest to Lagrangian studies that potentially use these data to study PSC formation (Engel et al., 2013; Hoyle et al., 2013; Grooß et al., 2014; Di Liberto et al., 2015). Here we used the AIRS data to evaluate explicitly resolved temperature fluctuations due to gravity waves in the European Centre for Medium-Range Weather Forecast (ECMWF) operational analysis for a set of 21 large-amplitude gravity wave events in the polar winter seasons. With the spatial resolution and physical representation of the forecast models improving over time as well as the inclusion of new observations within the assimilation procedures, it is important to know how realistically the analysis captures atmospheric gravity waves. As a second application, we performed a survey of joint AIRS gravity wave observations and PSC observations from the Michelson Interferometer for Passive Atmospheric Sounding (MIPAS) instrument (Fischer et al., 2008) aboard ESA's Envisat satellite. The survey covers the time period from 2003 to 2012, while Envisat MIPAS was in operation and provided nearly continuous monitoring of PSCs throughout the polar stratosphere. The main aim of this survey is to infer if the new AIRS data set introduced here can help to better identify gravity wave-induced PSC formation events and to stimulate more detailed Lagrangian case studies in future work.

In Sect. 2 we provide a description of the AIRS instrument and the method used to extract gravity wave information from the measurements. The spatial and temporal patterns of wave activity in the lower stratosphere at mid and high latitudes as observed by AIRS are discussed in Sect. 3. The evaluation of explicitly resolved temperature fluctuations in the ECMWF operational analysis is presented in Sect. 4. We discuss selected examples and the survey of gravity wave-induced PSC formation events based on AIRS and MIPAS data in Sect. 5. Finally, a summary and conclusions are given in Sect. 6.

2 AIRS observations of stratospheric gravity waves

AIRS (Aumann et al., 2003; Chahine et al., 2006) is one of six instruments aboard NASA's Aqua satellite. Aqua was launched in May 2002 into a nearly polar, low earth orbit at 705 km altitude, 100° inclination, and 100 min orbital period. The Aqua orbit is sun-synchronous, with Equator crossings at 01:30 LT (descending nodes) and 13:30 LT (ascending nodes). Nearly global coverage is achieved during 14.4 orbits per day. AIRS measures infrared radiance spectra in a cross-track scanning geometry. Each scan consists of 90 footprints and covers 1780 km ground distance. The footprint size varies between $14 \times 14\,km^2$ at nadir and $21 \times 42\,km^2$ at the scan extremes. Adjacent scans are separated by 18 km along-track distance. The spectral measurements cover the $3.74 - 15.4\,\mu m$ wavelength range in three bands. Brightness temperature measurements in the 4.3 and $15\,\mu m$ wavebands of CO_2 are particularly suited to study stratospheric gravity waves (e. g., Alexander and Barnet, 2007; Hoffmann and Alexander, 2009; Gong et al., 2012; Hoffmann et al., 2014).

For this study, we identified a set of 21 AIRS channels in the 15 μm CO_2 waveband to study gravity wave activity in the polar lower stratosphere. Our channel selection differs from earlier work of Hoffmann et al. (2013, 2014), which used AIRS channels in the 4.3 μm CO_2 waveband to obtain gravity wave information for the mid and upper stratosphere. The channels selected for this study are listed in Table 1, together with centroid frequencies and noise estimates (referred to as noise equivalent delta temperature, NeDT) at 250 K scene temperature. The radiance measurements of the selected channels are averaged to obtain a low-noise data product. Figure 1 shows the corresponding spectral mean temperature weighting functions for different atmospheric conditions and for different viewing directions of AIRS. The weighting function for polar winter conditions at nadir shows maximum sensitivity to stratospheric temperatures around 23 km altitude. Its full-width at half-maximum is 15 km and extends over the altitude range from 17 to 32 km, which provides overlap with the altitude range typically covered by PSCs (Poole and Pitts, 1994; Spang et al., 2005; Pitts et al., 2009). Comparing the weighting function for nadir and the outermost scan angles we found that both have nearly the same width, but that the latter is shifted upward by about 2 km. This shift is due to opacity growing more rapidly with altitude along slant ray paths. As stratospheric temperatures increase with altitude, measured radiances also increase with increasing scan angles, which is referred to as 'limb-brightening effect'. Although we are mainly interested in polar winter conditions, we also calculated weighting functions for polar summer conditions to assess the influence of atmospheric variability. In polar summer the temperature weighting functions are slightly broader and shift upward by about 2 km. This is due to stratospheric air density being higher in polar summer than in polar winter.

The temperature weighting functions can be used to calculate the amplitude response of the AIRS observations to gravity waves with different vertical wavelengths. Following the approach of Hoffmann and Alexander (2010) and Hoffmann et al. (2014), we convolve plane wave temperature perturbation profiles with known amplitude and vertical wavelength with the AIRS weighting functions. This provides simulated brightness temperature perturbations. Then the response is calculated as the ratio of the simulated brightness temperature perturbations and the true temperature amplitudes of the gravity waves. The amplitude response curves for the AIRS 15 μm data set are shown in Fig. 1. The AIRS observations are limited to gravity waves with long vertical wavelengths due to the broad weighting functions of the nadir observation geometry. The amplitude response is about 10, 20, and 50% for vertical wavelengths of about 15, 20, and 37 km, respectively. For instance, assuming gravity waves with a vertical wavelength of 20 km, this means that the brightness temperature amplitudes are damped by a factor of 5 in the AIRS observations compared to the real temperature amplitudes of the gravity waves. For smaller vertical wavelengths the attenuation will be stronger. As a consequence, brightness temperatures need to be measured with high precision to reliably detect the small perturbations caused by gravity waves. Reducing the measurement noise by spectrally averaging the radiance measurements of multiple AIRS channels helps to improve the response to gravity waves with short vertical wavelengths. Figure 1 shows that the amplitude response varies with respect to the atmospheric conditions, but that there are nearly no variations with respect to the AIRS scan angle.

Slowly-varying background signals need to be removed to extract gravity wave signals from the AIRS measurements. Background signals are caused by large-scale temperature gradients and planetary waves, but also by the limb-brightening effect. A standard detrending technique for AIRS is to remove the background defined by means of a polynomial fit to the brightness temperature measurements of each across-track scan (Wu, 2004; Eckermann et al., 2006; Alexander and Barnet, 2007;

Hoffmann et al., 2014). Usually a 4th-order polynomial is applied for this purpose. However, we identified problems with this approach in this study. Large-scale temperature gradients at the edge of the polar vortex can become rather large in the lower stratosphere and are sometimes not completely captured by the 4th-order polynomial. Therefore we replaced the 4th-order polynomial by a 6th-order polynomial, noting that the higher-order fit is still well constrained by the measurements. The 6th-order polynomial fit reduces the amplitude response to gravity waves with long horizontal wavelengths, but it also effectively removes unwanted temperature residuals near the polar vortex edge. Following Hoffmann et al. (2014), we estimated amplitude response levels of 50, 20, and 10% at 900, 1160, and 1350 km across-track wavelength, respectively (see Fig. 2). The limit for short horizontal wavelengths varies between 30 and 80 km, depending on the AIRS scan angle.

The analysis of AIRS gravity wave observations requires careful characterization of measurement noise. Accurate noise estimates are particularly important if brightness temperature variances are calculated for long time periods or large regions because gravity wave signals tend to average out in this case. We applied the approach of Hoffmann et al. (2014) to estimate the noise of the AIRS 15 μm brightness temperature data set directly from the measurements. Figure 3 shows that the noise estimates vary with scene temperature. The noise typically ranges from 0.109 K at 250 K scene temperature to 0.201 K at 195 K scene temperature. The highest noise is found in polar winter conditions, where scene temperatures are coldest and measured radiance signals are lowest. In contrast, lowest noise occurs in polar summer conditions. Note that the noise of the spectrally averaged data set is about 4 – 6 times lower than the nominal noise levels of the individual AIRS channels (Table 1). This provides a substantial improvement in terms of sensitivity to gravity waves with short vertical wavelengths. Note also that the dependence of noise on the scene temperature is well characterized by a Planck scaling curve (Fig. 3). Following Hoffmann et al. (2014), this scaling curve is used in our analyses to subtract noise estimates from brightness temperature variances, so that only gravity wave signals remain. The variances are then referred to as 'noise-corrected'. The correction has an accuracy of about 2%, which is determined by the uncertainty of fit of the Planck function.

As an example, Fig. 4 shows AIRS measurements at both 8.1 and 15 μm wavelength on 24 August 2004. This particular day is characterized by rather strong gravity wave activity at southern mid and high latitudes. The 15 μm brightness temperature map shows large-scale temperature gradients and planetary wave activity associated with the polar vortex. The limb-brightening effect is also visible, yielding increased brightness temperatures toward the scan edges. Gravity waves are hardly visible in the raw 15 μm brightness temperature map, but are isolated by means of the detrending method. The 15 μm brightness temperature perturbation map reveals gravity wave activity over the Southern Andes as well as the Transantarctic Mountains and Mac Robertson Land. Previous climatological studies using AIRS data showed that these regions are in fact hotspots of stratospheric gravity wave activity (Gong et al., 2012; Hoffmann et al., 2013, 2016a). AIRS measurements in the spectral window region at 8.1 μm can be used to detect storm systems (Aumann et al., 2006; Hoffmann and Alexander, 2010). The 8.1 μm brightness temperature map indicates several intense storm systems over the southern oceans, with cloud top temperatures as low as 210 – 230 K. However, the 15 μm brightness temperature map shows that these storm systems do not cause any direct radiance signals in the stratospheric channels. Note that this only applies for mid and high latitudes. At low latitudes the tropopause is higher and clouds can reach the altitude range covered by the selected channels. Our data should not be used at low latitudes.

Figure 4 also shows detrended and noise-corrected $15\,\mu$m brightness temperature variances on a $4° \times 2°$ longitude-latitude grid calculated from the brightness temperature perturbations. Although AIRS already provides about 80% global coverage during 12 h time intervals, we decided to combine data over a 24 h time window to close data gaps and homogenize temporal coverage. The $4° \times 2°$ grid boxes typically contain $160 - 520$ footprints at mid and high latitudes, which allows us to calculate variances with quite low sampling errors. Although AIRS provides measurement coverage up to the poles, any data beyond $\pm 85°$ latitude are excluded in this analysis. This is simply because the sampling coverage on a longitude-latitude grid decreases rapidly towards the poles. This could be mitigated by changing to another sampling grid, but we did not find this to be important because gravity wave activity beyond $\pm 85°$ latitude usually is rather low in the AIRS observations. Figure 4 shows that the variance map captures the individual gravity wave events found in the perturbation map. It also reveals that the noise correction very effectively suppresses noise signals in the variances. The map plot suggests that gravity wave signals can be reliably detected for variances as low as $5 \times 10^{-3}\,\mathrm{K}^2$. Variances below this threshold can be affected by sampling errors. Note that based on an estimated 2% uncertainty of the noise correction, the corresponding uncertainty of the variances is in the range of $2.4 \times 10^{-4}\,\mathrm{K}^2$ at 250 K scene temperature and $7.8 \times 10^{-4}\,\mathrm{K}^2$ at 195 K scene temperature, which is well below the sampling error. We calculated the gridded $15\,\mu$m brightness temperature variances on the $4° \times 2°$ grid on a daily basis for the entire $2003 - 2012$ time period for further analyses.

3   Temporal and spatial patterns of gravity wave activity

In this section we discuss the spatial and temporal patterns of the gravity wave activity in the lower stratosphere at mid and high latitudes as observed by AIRS during the years 2003 to 2012. First, we focus on daily variations. Figure 5 shows time series of detrended and noise-corrected $15\,\mu$m brightness temperature variances integrated over $85°\mathrm{S} - 55°\mathrm{S}$ and $55°\mathrm{N} - 85°\mathrm{N}$, respectively. As gravity wave activity typically occurs rather locally (cf. Fig. 4), the variances calculated for such large regions decrease to low levels. Maxima in different years range from 4.6×10^{-3} to $1.0 \times 10^{-2}\,\mathrm{K}^2$ in the northern hemisphere and 7.2×10^{-3} to $2.1 \times 10^{-2}\,\mathrm{K}^2$ in the southern hemisphere. However, note that these values are still considerably larger than the uncertainties of the noise correction. Figure 5 reveals that the daily variations of the gravity wave activity are substantial. Nevertheless, after detrending the daily time series with a 30-day running mean, the mean autocorrelation for a time lag of one day is 0.63 in the northern hemisphere and 0.57 in the southern hemisphere. The interannual variation of the autocorrelation is ± 0.16 in the northern hemisphere and ± 0.14 in the southern hemisphere. Despite the variability of the time series, this indicates that there is some persistence of gravity wave activity, which we attribute to the persistence of both the gravity wave sources and the tropospheric and stratospheric background winds. Another remarkable feature of the time series displayed in Fig. 5 are the sudden stratospheric warmings, most notably the northern hemisphere major warming in January 2009. It is associated with a reversal of ERA-Interim 30 hPa zonal winds from $+30$ to -15 m/s, an increase of 60 hPa temperatures from 200 to 230 K, and a decrease of observed gravity wave activity to almost zero.

The time series for both the northern and southern hemisphere in Fig. 5 show a distinct seasonal cycle of gravity wave activity with maxima in the winter months. Gravity wave activity is typically stronger and lasts longer in the southern hemisphere,

whereas the interannual variability and the intraseasonal variations are larger in the northern hemisphere. A statistical analysis of the seasonal cycle of gravity wave activity is presented in Fig. 6. We calculated the 10, 25, 50, 75, and 90% quantiles of the 15 μm brightness temperature variance distributions for 30-day time windows. The analysis was performed with the time windows being centered around the beginning or the middle of each month. Based on the 10% and 90% quantiles, we found that the seasonal cycle of gravity wave activity in the northern hemisphere typically begins in November and ends sometime in February to April. The cycle lasts about $2-6$ months. Maximum activity occurs during January. In the southern hemisphere the cycle begins in April to June and ends in November or December. The cycle lasts about $5-9$ months. Maximum activity occurs during August. Figure 6 also shows occurrence frequencies f_{NAT} of ERA-Interim 60 hPa temperatures falling below $T_{NAT} = 195$ K. This allows us to compare the typical timing of synoptic-scale PSC occurrence to the timing of gravity wave activity. In the southern hemisphere the seasonal cycle of gravity wave activity lasts slightly longer than the cycle of PSC activity, suggesting that wave-induced PSC formation is particularly important in fall and spring. The Arctic polar vortex is considerably warmer than the Antarctic polar vortex and gravity waves may be an even more important source of PSCs in this case. We found values of f_{NAT} of up to 10% for the northern hemisphere and up to 65% for the southern hemisphere. Furthermore, Fig. 6 also shows occurrence frequencies f_{OBS} of ERA-Interim 30 hPa zonal winds exceeding a threshold of 20 m/s. This is a proxy for conditions that are linked to unidirectional and strongly increasing winds with height, which is a requirement for the occurrence of gravity waves with long vertical wavelengths that are best visible to AIRS. From f_{OBS} we can infer a time window in which the atmospheric conditions are most suitable for AIRS to detect gravity waves. This time window is significantly longer than the window of synoptic-scale PSC activity.

For comparison, we also analyzed the seasonal cycle for two orographic hotspots of gravity wave activity, the Scandinavian Mountains and the Antarctic Peninsula (Fig. 6). Local variances at the hotspots are much larger than the polar averages. For instance, the local maximum of the 90% quantile exceeds the polar average by a factor of 9 for the Antarctic Peninsula and by a factor of 4 for the Scandinavian Mountains. The variance distributions for the hotspots show positive skewness, with a long tail towards large variances, as can be seen by comparing the ranges between the 10% and 90% quantiles and the median. This indicates that few, but strong mountain wave events contribute substantially to gravity wave activity at these hotspots. Figure 5 shows that both the 60 hPa temperatures and 30 hPa zonal winds vary much more locally at the hotspots compared with the polar regions as a whole, in particular in the northern hemisphere. The local variations of the zonal wind increase the chance for AIRS gravity wave observations at the hotspots compared with the polar regions. The maximum of f_{OBS} is close to 100% for the Antarctic Peninsula, 75% for the southern hemisphere, 82% for the Scandinavian Mountains, and 53% for the northern hemisphere. The maximum PSC occurrence frequencies f_{NAT} at the hotspots are only slightly lower ($2-5$ percentage points) than those for the polar regions. However, we note that the onset of synoptic-scale PSC formation at the Antarctic Peninsula is in June, which is a month later compared with the southern hemisphere polar region. Gravity wave activity at the Antarctic Peninsula starts as early as April. This further stresses the important role of the Antarctic Peninsula for gravity wave-induced PSC formation.

In order to analyze the spatial patterns and to identify source regions of gravity wave activity we calculated monthly variances on the $4° \times 2°$ longitude-latitude grid directly from the daily data. In Figs. 7 and 8 we also show maps of terrain height

standard deviations calculated from a 2-minute gridded global relief data set (ETOPO2v2; National Geophysical Data Center, 2006) to indicate possible orographic sources of gravity wave activity. The AIRS maps indicate that gravity wave activity increases significantly at a number of orographic hotspots. In the northern hemisphere this includes (from west to east) the Arctic Archipelago, Labrador, Greenland, Iceland, the United Kingdom, the Alps, the Scandinavian Mountains, the Ural Mountains, the Altai Mountains, the Central Siberian Plateau, and the East Siberian Plateau. Gravity wave activity over the Rocky Mountains is largely absent, which is due to relatively low stratospheric background winds over this mountain range (Hoffmann et al., 2013, 2014). In the southern hemisphere we found increased gravity wave activity in a latitude band around $70°S - 50°S$ during the winter months, which is attributed mostly to jet and storm sources (Sato et al., 2012; Hendricks et al., 2014; Hindley et al., 2015). Orographic hotspots can be identified at the southern Andes, the Antarctic Peninsula, South Georgia, Kerguelen Islands, and the Transantarctic Mountains. As there is large variability of gravity wave activity, in particular in the northern hemisphere, we calculated standard errors of the monthly means shown in Figs. 7 and 8 to assess if they are representative. We found standard errors of $29 - 39\%$ for the months from November to February for the northern hemisphere and $18 - 21\%$ for the months from May to October for the southern hemisphere. The spatial patterns of gravity wave activity in the lower stratosphere found here agree well with those identified by Gong et al. (2012) and Hoffmann et al. (2013, 2014, 2016a) for the mid and upper stratosphere.

Strong background winds in the stratosphere tend to go along with unidirectional and increasing winds with height (e. g., Orr et al., 2010). In this case wave refraction will result in long vertical wavelengths (e. g., Wu and Eckermann, 2008), which are best visible to AIRS. On the contrary, weak background winds are associated with gravity waves with short vertical wavelengths, which are generally not detectable by AIRS. This combined effect of the stratospheric background winds and the vertical wavelength sensitivity of AIRS is referred to as an 'observational filter' (Alexander and Barnet, 2007; Hoffmann et al., 2014, 2016a). Figures 7 and 8 also show contours of ERA-Interim monthly mean zonal winds at $30\,hPa$. The $30\,hPa$ level (about $25\,km$ altitude) is close to the altitude range where the AIRS observations provide maximum sensitivity to stratospheric temperatures. Figures 7 and 8 indicate that the $30\,hPa$ zonal winds have a significant influence on the observability of gravity waves with AIRS. For both the northern and southern hemisphere we found that strong westerlies are a prerequisite for the observation of gravity wave activity with AIRS. The comparison suggests that zonal winds need to exceed levels of about $10 - 20\,m\,s^{-1}$ before gravity wave activity becomes visible in the AIRS data. This shows that the observational filter needs to be taken into account in the analysis of AIRS gravity wave observations.

4   Evaluation of temperature fluctuations in the ECMWF operational analysis

In this study we used the new AIRS data set to evaluate explicitly resolved temperature fluctuations due to gravity waves in the ECMWF operational analysis. During the time period considered here ($2003 - 2012$) the horizontal resolution of the ECMWF operational analysis was increased from T511 ($39\,km$ effective resolution) to T1279 ($16\,km$), the number of model levels was increased from 60 to 91, and the model top was raised from 0.1 to 0.01 hPa. The typical vertical resolution is about $0.5 - 1.1\,km$ at $15 - 30\,km$ altitude. We here considered analysis data at 0 and 12 UTC and forecast data at 3, 6, 9, 15, 18, and

21 UTC. AIRS radiance data have been used for operational forecasting since October 2003 (McNally et al., 2006; Dee et al., 2011). Observations of up to 210 channels are used in the assimilation procedure, of which 10 are also considered in our AIRS data product. The comparisons of AIRS and ECMWF data presented here are therefore not strictly based on independent data and should be considered as an 'evaluation' rather than a 'validation'. However, the assimilation of AIRS data at ECMWF

5 is restricted to cloud-free scenes and an additional random thinning operation is applied to ensure a minimum horizontal spacing of 120 km between the footprints. This poses a Nyquist limit of 240 km on horizontal wavelengths regarding the direct assimilation of small-scale gravity waves from AIRS observations into the analysis. Wave patterns with shorter horizontal wavelengths are most likely generated by the model itself.

In our comparison we took the effects of radiative transfer and the AIRS satellite observation geometry into account. First,

10 we extracted temperature profiles from the ECMWF data at the locations of individual satellite footprints by means of 3-D linear interpolation. Next, we convolved the temperature profiles with the weighting function of the selected channels. This gave us simulated brightness temperature measurements on the AIRS measurement grid. Gravity wave signals were then extracted by means of the same detrending procedure as used for the real AIRS data. The main difficulty in this comparison is related to the coarse time resolution (3-hourly) at which the ECMWF data are provided. We tested different interpolation

15 schemes (nearest neighbor, linear, and cubic), but found that temporal interpolation often does not provide physically meaningful solutions for gravity waves that may propagate through the troposphere and stratosphere within just a few hours. Therefore we decided to avoid time interpolation altogether and to perform the analysis directly with the meteorological data at the 3 h synoptic time steps. Daily gravity wave variances were calculated using the data of all synoptic time steps on each day. This approach introduces some uncertainty in the analysis, but it was found to still provide the best overall agreement with real

20 AIRS observations.

As an example, Fig. 9 shows a qualitative comparison of 15 µm brightness temperature perturbations from real AIRS measurements and corresponding simulated measurements based on the ECMWF operational analysis data. Real measurements shown here were obtained on 12 December 2003, 12:00 to 24:00 UTC in the northern hemisphere and 22 July 2011, 00:00 to 12:00 UTC in the southern hemisphere. The simulated measurements apply to 18:00 and 06:00 UTC synoptic time on these

25 days, respectively. The AIRS measurements in the northern hemisphere show mountain waves near the east coast of Greenland as well as the Scandinavian Mountains. There is also a band of wave activity around 60 – 75°N extending over large parts of Asia. The wave activity in this region can be attributed to orography, but also to jet and storm sources. The example for the southern hemisphere shows strong mountain waves at the southern Andes. The measurements also reveal non-orographic wave activity related to jet and storm sources possibly mixed with orographic waves near coastal East Antarctica at 50 – 70°S and

30 60°E – 120°W. The qualitative comparison shows that both orographic and non-orographic waves are captured by the ECMWF operational analysis to a great extent, i. e., there is remarkably good agreement between the regions where gravity waves were represented in the analysis and where they actually occurred. Despite the time differences, even the details of the wave patterns look similar, in particular for the southern hemisphere example in July 2011. The improved horizontal resolution of the ECMWF operational analysis is the likely reason why individual patterns are better captured in the southern hemisphere exam-

ple for the year 2011 compared to the northern hemisphere example for the year 2003. However, we note that wave amplitudes from the simulations are lower than the wave amplitudes from the AIRS measurements in both examples.

To quantify the systematic differences between the wave amplitudes in the AIRS observations and the meteorological analyses we analyzed seasonal peak events. We selected the day with the largest gravity wave variance from the AIRS time series (Fig. 5) for each winter season in the northern and southern hemisphere. Figure 10 shows a bar chart of 15 μm brightness temperature standard deviations for these peak events, calculated from the detrended and noise-corrected 15 μm brightness temperature variances shown in Fig. 5. Here we present standard deviations rather than variances, because those can be related more directly to gravity wave amplitudes. Figure 10 shows that the simulated wave amplitudes almost always underestimate observed wave amplitudes. On average, the ECMWF operational analysis reproduces $(32 \pm 13)\%$ of the observed standard deviations in the northern hemisphere and $(47 \pm 22)\%$ for the southern hemisphere. Commonly, gravity wave amplitudes are better reproduced in the southern hemisphere than in the northern hemisphere. This difference between the hemispheres is related to differences of the typical gravity wave spectra in both hemispheres. For the 21 peak events analyzed here, a 2-D spectral analysis of the AIRS data using the S-Transform method (Stockwell et al., 1996; Alexander and Barnet, 2007) yielded mean horizontal wavelengths of (116 ± 52) km in the northern hemisphere and (133 ± 72) km in the southern hemisphere. These differences might be due to the gravity wave sources such as orography, convection, and jets as well as differences of the background flow between the hemispheres. The model produces shorter horizontal wavelength waves in the northern hemisphere, however, the wavelengths were overall longer than AIRS, and we found stronger attenuation of the wave amplitudes in the model. We attribute the interannual variability of the scaling factors of the wave amplitudes between the AIRS and ECMWF data to atmospheric variability, but also to improvements in the spatial resolution, the forecast model, and the data assimilation system of the operational analysis over time.

5 A survey of gravity wave-induced PSC formation events

In this section we present a survey of joint AIRS gravity wave and Envisat MIPAS PSC observations during the years 2003 to 2012. Like Aqua, Envisat operated in a nearly polar, low earth orbit (790 km altitude, 98° inclination, 101 min orbital period) with Equator crossings at 10:00 LT and 22:00 LT. Envisat MIPAS (Fischer et al., 2008) measured $4.15 - 14.6 \mu$m limb emission spectra of atmospheric constituents from the mid troposphere to the mesosphere at high spectral resolution. Nominal measurements in the 'full resolution' phase (0.025 cm^{-1} spectral resolution) in $2002 - 2004$ provided 550 km horizontal sampling and 3 km vertical sampling in the lower stratosphere. This was improved to 410 km and $1.5 - 2$ km in the 'optimized resolution' phase (0.0625 cm^{-1}) in $2005 - 2012$. The instantaneous field of view of MIPAS covers $3 - 4$ km (elevation) $\times$ 30 km (azimuth). Several studies demonstrated that MIPAS was capable of detecting PSCs based on specific spectral signatures in the mid infrared (Spang et al., 2004, 2005; Höpfner et al., 2006a, b; Spang et al., 2012). A particular advantage of MIPAS was its sensitivity to low particle concentrations due to the long integration paths of the limb observation geometry. Here we make use of a new MIPAS PSC data product introduced by Spang et al. (2016), which uses radiance measurements at 7.1, 8.2, 10.5, 12.0, and 12.7 μm to detect PSCs and to classify between different particle types. The new method has been developed

and tested with a database of radiative transfer model calculations of realistic PSC particle size distributions, geometries, and composition. The detection and classification results were compared with space-borne lidar observations. Spang et al. (2016) showed that ice particles are classified most accurately with the new method.

Our survey of gravity wave-induced PSC formation events is based on daily maps of detrended and noise-corrected AIRS 15 μm brightness temperature variances and MIPAS PSC detections. Selected examples of these maps are shown in Fig. 11. MIPAS PSC detections are shown for the altitude range of about $18-22$ km ($450-550$ K potential temperature), which coincides with the range of polar vortex temperature minima (Randel et al., 2004) and PSC occurrence frequency maxima (Poole and Pitts, 1994; Spang et al., 2005; Pitts et al., 2009) during the course of the polar winter. To help link the PSC observations to gravity wave activity, further information was added to the maps, following Spang et al. (2016). PSC existence temperatures were estimated following Hanson and Mauersberger (1988) and Marti and Mauersberger (1993), based on ERA-Interim pressure and temperature data at the 500 K isentropic level as well as typical stratospheric values for HNO_3 (9 ppbv) and H_2O (4 ppmv). PSC detections associated with synoptic-scale temperatures significantly larger than the specific existence temperature are candidates for gravity wave-induced formation events. Furthermore, the maps include contours of the Montgomery streamfunction (calculated from ERA-Interim data), representing streamlines of the geostrophic wind at the 500 K isentropic level. The streamfunctions illustrate the flow of air masses on short time scales and can be used to infer if the MIPAS PSC detections occurred downstream of AIRS gravity wave observations. Alexander et al. (2011) and Alexander et al. (2013) already highlighted the importance of advection of PSCs away from the regions where temperature perturbations were observed. The streamfunction approach helps to overcome difficulties related to the miss-times between the Aqua and Envisat overpasses and the synoptic time steps of the meteorological data.

Figure 11 shows two examples of gravity wave-induced PSC formation events in the northern hemisphere. On 25 January 2007, MIPAS detected ice PSCs over Scandinavia at synoptic-scale temperatures up to $6-9$ K above T_{ice}. These detections are associated with weak gravity wave activity observed by AIRS over the Scandinavian Mountains. On 7 January 2011, MIPAS detected ice, STS, and NAT PSCs over the Arctic Archipelago at synoptic-scale temperatures about 3 K above T_{NAT}. Although the Arctic Archipelago was found to be a gravity wave hotspot in the northern hemisphere (Sect. 3), no indication for gravity wave activity is seen in this region on this particular day in the AIRS data. A reason might be that 30 hPa horizontal wind speeds directly above the MIPAS detections are relatively low (about $35-45$ m/s) compared with other cases we looked at. The AIRS observational filter causes stronger attenuation of the observed wave amplitudes in this case. Gravity wave activity is observed $3-6$ h upstream over the Beaufort Sea where horizontal wind speeds increase. Figure 11 also presents three examples of gravity wave-induced PSC formation in the southern hemisphere. The measurements on 8 July 2007 show a rather typical example of the formation of ice PSCs due to mountain waves at the Antarctic Peninsula. The ice PSCs are formed at synoptic-scale temperatures up to $4-10$ K above T_{ice}. NAT particles are observed further downstream of the Antarctic Peninsula, which is consistent with the ice particles serving as condensation nuclei for NAT formation (Carslaw et al., 1998a; Höpfner et al., 2006b; Eckermann et al., 2009). Although mountain wave activity is most frequent at the Antarctic Peninsula (Hoffmann et al., 2016a), other orographic features in Antarctica can also play a role in PSC formation. The AIRS and MIPAS observations

on 25 July 2008 and 29 August 2008 show cases of mountain wave-induced formation of ice PSCs over the Transantarctic Mountains and near Enderby Land and Mac Robertson Land, respectively.

In Figure 11 we displayed $15\,\mu$m brightness temperature variances up to a level of $0.075\,\mathrm{K}^2$. A relatively low cut-off was selected here to make also weak wave signals visible. Following the approach of Alexander and Grimsdell (2013), we per-

5 formed a cross check for the orographic wave events to confirm that these are indeed cases with substantial true gravity wave amplitudes. We computed the vertical wavelength λ_z from the gravity wave dispersion relation for stationary waves, assuming that the ground-based frequency and phase speed are zero,

$$\lambda_z = 2\pi \left[\left(\frac{N}{u} \right)^2 - \left(\frac{2\pi}{\lambda_x} \right)^2 \right]^{-0.5}. \tag{1}$$

Here $N \approx 0.02\,\mathrm{s}^{-1}$ refers to the stratospheric buoyancy frequency. The background wind speed u was taken from the ERA-

10 Interim reanalysis at 30 hPa. The horizontal wavelength λ_x was determined by means of spectral analysis of the AIRS data. The vertical wavelength estimate λ_z was used to determine the amplitude response R from the data shown in Fig. 1. Then R was used to estimate the true gravity wave amplitude T' from the measured brightness temperature amplitude BT', according to $T' = BT' R^{-1}$. The results of the calculations for the four orographic wave events in Fig. 11 are summarized in Table 4. Based on background wind speeds of about $55 - 65\,\mathrm{m\,s}^{-1}$ at 30 hPa and horizontal wavelengths of about $95 - 130$ km, we found vertical

15 wavelengths of about $17 - 21$ km. The corresponding amplitude response is about $15 - 22\%$. Brightness temperature amplitudes of about $1.3 - 2.6$ K scale to true gravity wave amplitudes of about $7 - 12$ K. Such large true amplitudes are indeed consistent with observations of ice PSCs well above the frost point.

As another cross check of the case studies shown in Fig. 11, we performed a comparison with PSC observations of the Cloud-Aerosol Lidar with Orthogonal Polarization (CALIOP) (Pitts et al., 2009; Winker et al., 2010) instrument. CALIOP

20 is an active lidar instrument that probes the vertical and along-track structure of aerosols and clouds with unprecedented spatial resolution, i. e., 180 m in vertical direction and 1.67 km in along-track direction at $20.2 - 30.1$ km altitude. Figure 12 shows CALIOP observations for the events on 25 January 2007 in the northern hemisphere and 8 July 2007 in the southern hemisphere. The CALIOP browse images in Fig. 12 indicate the presence of PSCs in close proximity of MIPAS detections of ice PSCs at $20 - 23$ km and $19 - 29$ km altitude, respectively. The 532 nm total attenuated backscatter shows maximum signals

25 up to $8 \times 10^{-3}\,\mathrm{km}^{-1}\,\mathrm{sr}^{-1}$. These large signals are a strong indicator for the presence of wave-induced ice particles. Note that stratospheric features can also be found in CALIOP observations for the three case studies not shown here. However, we note that in these cases the backscatter signals are weaker and may be caused by other types of PSC particles.

We also conducted backward trajectory calculations to confirm that the MIPAS detections of ice PSC are not related to synoptic-scale temperatures falling below T_{ice}, which suggests that gravity waves play a role in PSC formation for these events.

30 The calculations were performed with the Lagrangian particle dispersion model introduced by Hoffmann et al. (2016b), using both ERA-Interim and the ECMWF operational analysis as meteorological input data. The calculations cover a time period of 24 h. We conducted the calculations for ensembles of 100 trajectories to take into account the broad measurement volume of MIPAS as well as atmospheric diffusion and subgrid-scale wind fluctuations. The results for two detections are presented in Fig. 13. We found that the mean temperatures of the air parcels are about $4 - 8$ K above T_{ice} at the beginning and raise by another

$15 - 25$ K towards the end of the simulations. This indicates that large-scale synoptic temperatures are likely not the reason for PSC formation. Furthermore, note that the temperature curve for the 25 January 2007 case study shows a wave-like signature with about $4 - 5$ K amplitude for the operational analysis and $1 - 2$ K for ERA-Interim during the first 3 h of the simulations. Considering the wave perturbations, the local temperature gets close to T_{ice} for the operational analysis. This provides more evidence that mountain waves over Scandinavia play an important role in PSC formation in this case. For all the cases presented in Fig. 11 we analyzed trajectory calculations for 22 MIPAS detections of ice PSCs that occurred above T_{ice}, but we did not found a case in which the temperatures along the trajectories dropped below T_{ice} for an extended period of time.

Based on the daily maps we performed a survey of all AIRS and MIPAS observations in the northern and southern polar winter seasons during the years 2003 to 2012. In this survey we identified 48 events of gravity wave-induced PSC formation (Tables 2 and 3), with 29 events being located in the southern hemisphere and 19 events being located in the northern hemisphere. This first survey suggests that formation events appear more frequently in the southern hemisphere than in the northern hemisphere. This is not consistent with studies showing that there are larger proportions of PSCs due to orographic gravity waves in the Arctic than in the Antarctic (Kohma and Sato, 2011; Alexander et al., 2013). However, our findings might be biased due to the more stable atmospheric conditions in the southern hemisphere that ease the identification of events by means of visual inspection of the AIRS and MIPAS maps and stronger winds in the southern hemisphere that make waves more visible in AIRS data. In the southern hemisphere, most events are found near the Antarctic Peninsula (20 events), followed by the Transantarctic Mountains (4), and other places of coastal Antarctica. In the northern hemisphere, most events are found near Greenland (5), Iceland (4), and the Scandinavian Mountains (4). The dates of the events and possible source regions of gravity wave activity are listed in Tables 2 and 3. The tables provide suggestions for possible case studies that could be exploited in future work, e. g., by means of Lagrangian trajectory analyses. The large number of events identified here is promising and supports the conclusion that gravity wave-induced PSC formation plays an important role in polar ozone chemistry. It shows that the AIRS record of gravity wave activity in the lower stratosphere is a valuable complementary resource that can be used to study this process in more detail.

6 Summary and conclusions

Here we introduced a new long-term satellite record of gravity wave activity in the lower stratosphere at mid and high latitudes. The data set was compiled to support studies on the influence of small-scale temperature fluctuations due to gravity waves on PSC formation. The record was derived from AIRS/Aqua observations between January 2003 and December 2012. Gravity wave activity is measured in terms of detrended and noise-corrected 15 μm brightness temperature variances on a daily basis. We discussed the characteristics of the AIRS channels selected for this analysis in terms of vertical coverage, wavelength sensitivity, and measurement noise. The analysis of temporal patterns of the AIRS gravity wave observations revealed a strong seasonal cycle with wintertime maxima at both northern and southern hemisphere mid and high latitudes. The analysis of spatial patterns showed that the wave activity is mostly related to orographic, jet, and storm sources. The observed patterns of wave activity agree well with those reported in other climatological studies of global gravity wave activity using AIRS observations

(Gong et al., 2012; Hoffmann et al., 2013, 2014). The observed gravity wave activity is closely correlated with zonal winds at the 30 hPa level, which we attribute to the AIRS observational filter. Typically, a background wind of at least $10-20\,\mathrm{m\,s^{-1}}$ is required to foster the propagation of gravity waves with long vertical wavelengths into the lower stratosphere, which are best visible to AIRS. Small vertical wavelengths are associated with significant attenuation of the observed brightness temperature perturbations. This attenuation needs to be taken into account if the AIRS data are compared with other measurements or model results. This can be achieved by convoluting temperature perturbation profiles from the comparative data with the AIRS weighting functions. Alternatively, the brightness temperature perturbations can be scaled up to estimate true wave amplitudes, but this requires information on vertical wavelength for any particular case.

We discussed two applications of the new AIRS long-term record of gravity wave activity. The first application is an evaluation of explicitly resolved gravity waves in the ECMWF meteorological data products. We found that observed and simulated gravity wave patterns agree well in extent and shape. However, the amplitudes of the short horizontal and long vertical wavelength gravity waves that are best visible to AIRS are typically underestimated by a factor of $2-3$ by the ECMWF operational analysis. This is in line with results of Schroeder et al. (2009) and Jewtoukoff et al. (2015), who validated temperature fluctuations and gravity wave momentum fluxes in the ECMWF operational analysis with Infrared limb sounding measurements and superpressure balloon observations, respectively. Both studies attributed the underestimation of gravity wave amplitudes and momentum fluxes to the spatial truncation of the ECMWF model. The second application presented here is a survey of gravity wave-induced PSC formation events based on joint AIRS and MIPAS observations. Envisat MIPAS observations during the years 2003 to 2012 revealed nearly 50 events of PSC detections at synoptic-scale temperatures well above the PSC existence and formation thresholds. In many cases we found that the detections occurred downstream of source regions with gravity wave activity as revealed by AIRS observations. The large number of events found in this survey confirms that gravity wave-induced PSC formation is indeed an important process in polar ozone chemistry. The events found here can be explored in more detail by means of Lagrangian trajectory analyses in future work.

7 Data availability

AIRS data are distributed by the NASA Goddard Earth Sciences Data Information and Services Center (AIRS Science Team and Chahine, 2007). CALIOP data are distributed by the NASA Langley Research Center Atmospheric Science Data Center. Envisat MIPAS Level-1B data are distributed by the European Space Agency. The ERA-Interim reanalysis (Dee et al., 2011) and the operational analysis were obtained from the European Centre for Medium-Range Weather Forecasts. The ETOPO2v2 data set was obtained from the US Department of Commerce, National Oceanic and Atmospheric Administration, National Geophysical Data Center (National Geophysical Data Center, 2006). Interested scientists can obtain access to the complete AIRS gravity wave data set introduced in this paper by contacting the leading author.

Acknowledgements. MJA and LAH acknowledge the NASA Goddard Space Flight Center for support (grant #NNX14AO76G).

References

AIRS Science Team and Chahine, M.: AIRS/Aqua L1B Infrared (IR) geolocated and calibrated radiances V005, version 005, available at: http://disc.gsfc.nasa.gov/datacollection/AIRIBRAD_005.html (last access: 31 December 2015), Greenbelt, MD, USA, Goddard Earth Sciences Data and Information Services Center (GES DISC), 2007.

5   Alexander, M. J. and Barnet, C. D.: Using satellite observations to constrain gravity wave parameterizations for global models, J. Atmos. Sci., 64, 1652–1665, 2007.

Alexander, M. J. and Grimsdell, A. W.: Seasonal cycle of orographic gravity wave occurrence above small islands in the Southern Hemisphere: Implications for effects on the general circulation, J. Geophys. Res., 118, 11 589–11 599, 2013.

Alexander, M. J. and Pfister, L.: Gravity wave momentum flux in the lower stratosphere over convection, Geophys. Res. Lett., 22, 2029–2032, 10   1995.

Alexander, S. P., Klekociuk, A. R., Pitts, M. C., McDonald, A. J., and Arevalo-Torres, A.: The effect of orographic gravity waves on Antarctic polar stratospheric cloud occurrence and composition, J. Geophys. Res., 116, D06109, doi:10.1029/2010JD015184, 2011.

Alexander, S. P., Klekociuk, A. R., McDonald, A. J., and Pitts, M. C.: Quantifying the role of orographic gravity waves on polar stratospheric cloud occurrence in the Antarctic and the Arctic, J. Geophys. Res., 118, 11,493–11,507, 2013.

15   Aumann, H. H., Chahine, M. T., Gautier, C., Goldberg, M. D., Kalnay, E., McMillin, L. M., Revercomb, H., Rosenkranz, P. W., Smith, W. L., Staelin, D. H., Strow, L. L., and Susskind, J.: AIRS/AMSU/HSB on the Aqua Mission: Design, Science Objective, Data Products, and Processing Systems, in: IEEE Trans. Geosci. Remote Sens., vol. 41, pp. 253–264, 2003.

Aumann, H. H., Broberg, S., Elliott, D., Gaiser, S., and Gregorich, D.: Three years of Atmospheric Infrared Sounder radiometric calibration validation using sea surface temperatures, J. Geophys. Res., 111, doi:10.1029/2005JD006822, 2006.

20   Baumgaertner, A. J. G. and McDonald, A. J.: A gravity wave climatology for Antarctica compiled from Challenging Minisatellite Payload/Global Positioning System (CHAMP/GPS) radio occultations, J. Geophys. Res., 112, D05103, doi:10.1029/2006JD007504, 2007.

Browell, E. V., Butler, C. F., Ismail, S., Robinette, P. A., Carter, A. F., Higdon, N. S., Toon, O. B., Schoeberl, M. R., and Tuck, A. F.: Airborne lidar observations in the wintertime Arctic stratosphere: Polar stratospheric clouds, Geophys. Res. Lett., 17, 385–388, 1990.

Campbell, J. R. and Sassen, K.: Polar stratospheric clouds at the South Pole from 5 years of continuous lidar data: Macrophysical, optical, 25   and thermodynamic properties, J. Geophys. Res., 113, doi:10.1029/2007JD009680, d20204, 2008.

Carslaw, K., Luo, B., Clegg, S., Peter, T., Brimblecombe, P., and Crutzen, P.: Stratospheric aerosol growth and HNO_3 gas phase depletion from coupled HNO_3 and water uptake by liquid particles, Geophys. Res. Lett., 21, 2479–2482, 1994.

Carslaw, K., Wirth, M., Tsias, A., Luo, B., Dörnbrack, A., Leutbecher, M., Volkert, H., Renger, W., Bacmeister, J., and Peter, T.: Particle microphysics and chemistry in remotely observed mountain polar stratospheric clouds, J. Geophys. Res., 103, 5785–5796, 1998a.

30   Carslaw, K. S., Wirth, M., Tsias, A., Luo, B. P., Dörnbrack, A., Leutbecher, M., Volkert, H., Renger, W., Bacmeister, J. T., Reimer, E., and Peter, T.: Increased stratospheric ozone depletion due to mountain-induced atmospheric waves, Nature, 391, 675–678, 1998b.

Chahine, M. T., Pagano, T. S., Aumann, H. H., Atlas, R., Barnet, C., Blaisdell, J., Chen, L., Divakarla, M., Fetzer, E. J., Goldberg, M., Gautier, C., Granger, S., Hannon, S., Irion, F. W., Kakar, R., Kalnay, E., Lambrigtsen, B. H., Lee, S., Marshall, J. L., McMillan, W. W., McMillin, L., Olsen, E. T., Revercomb, H., Rosenkranz, P., Smith, W. L., Staelin, D., Strow, L. L., Susskind, J., Tobin, D., Wolf, W., and 35   Zhou, L.: AIRS: improving weather forecasting and providing new data on greenhouse gases, B. Am. Meteorol. Soc., 87, 911–926, 2006.

Dee, D. P., Uppala, S. M., Simmons, A. J., Berrisford, P., Poli, P., Kobayashi, S., Andrae, U., Balmaseda, M. A., Balsamo, G., Bauer, P., Bechtold, P., Beljaars, A. C. M., van de Berg, L., Bidlot, J., Bormann, N., Delsol, C., Dragani, R., Fuentes, M., Geer, A. J., Haimberger, L.,

Healy, S. B., Hersbach, H., Hólm, E. V., Isaksen, L., Kållberg, P., Köhler, M., Matricardi, M., McNally, A. P., Monge-Sanz, B. M., Morcrette, J.-J., Park, B.-K., Peubey, C., de Rosnay, P., Tavolato, C., Thépaut, J.-N., and Vitart, F.: The ERA-Interim reanalysis: configuration and performance of the data assimilation system, Quart. J. Roy. Meteorol. Soc., 137, 553–597, 2011.

Di Liberto, L., Lehmann, R., Tritscher, I., Fierli, F., Mercer, J. L., Snels, M., Di Donfrancesco, G., Deshler, T., Luo, B. P., Grooß, J.-U., Arnone, E., Dinelli, B. M., and Cairo, F.: Lagrangian analysis of microphysical and chemical processes in the Antarctic stratosphere: a case study, Atmos. Chem. Phys., 15, 6651–6665, 2015.

Dörnbrack, A., Leutbecher, M., Kivi, R., and Kyrö, E.: Mountain-wave-induced record low stratospheric temperatures above northern Scandinavia, Tellus, 51, 951–963, 1999.

Dörnbrack, A., Birner, T., Fix, A., Flentje, H., Meister, A., Schmid, H., Browell, E. V., and Mahoney, M. J.: Evidence for inertia gravity waves forming polar stratospheric clouds over Scandinavia, J. Geophys. Res., 107, doi:10.1029/2001JD000452, 2002.

Durran, D. R. and Klemp, J. B.: Another look at downslope winds. Part II: nonlinear amplification beneath wave-overturning layers, J. Atmos. Sci., 44, 3402–3412, 1987.

Eckermann, S. D., Wu, D. L., Doyle, J. D., Burris, J. F., McGee, T. J., Hostetler, C. A., Coy, L., Lawrence, B. N., Stephens, A., McCormack, J. P., and Hogan, T. F.: Imaging gravity waves in lower stratospheric AMSU-A radiances, Part 2: Validation case study, Atmos. Chem. Phys., 6, 3343–3362, 2006.

Eckermann, S. D., Hoffmann, L., Höpfner, M., Wu, D. L., and Alexander, M. J.: Antarctic NAT PSC belt of June 2003: Observational validation of the mountain wave seeding hypothesis, Geophys. Res. Lett., 36, L02807, doi:10.1029/2008GL036629, 2009.

Engel, I., Luo, B. P., Pitts, M. C., Poole, L. R., Hoyle, C. R., Grooß, J.-U., Dörnbrack, A., and Peter, T.: Heterogeneous formation of polar stratospheric clouds – Part 2: Nucleation of ice on synoptic scales, Atmos. Chem. Phys., 13, 10 769–10 785, 2013.

Fischer, H., Birk, M., Blom, C., Carli, B., Carlotti, M., von Clarmann, T., Delbouille, L., Dudhia, A., Ehhalt, D., Endemann, M., Flaud, J. M., Gessner, R., Kleinert, A., Koopman, R., Langen, J., López-Puertas, M., Mosner, P., Nett, H., Oelhaf, H., Perron, G., Remedios, J., Ridolfi, M., Stiller, G., and Zander, R.: MIPAS: an instrument for atmospheric and climate research, Atmos. Chem. Phys., 8, 2151–2188, 2008.

Fritts, D. C. and Alexander, M. J.: Gravity wave dynamics and effects in the middle atmosphere, Rev. Geophys., 41, 1003, doi:10.1029/2001RG000106, 2003.

Gong, J., Wu, D. L., and Eckermann, S. D.: Gravity wave variances and propagation derived from AIRS radiances, Atmos. Chem. Phys., 12, 1701–1720, 2012.

Grimsdell, A. W., Alexander, M. J., May, P. T., and Hoffmann, L.: Model study of waves generated by convection with direct validation via satellite, J. Atmos. Sci., 67, 1617–1631, 2010.

Grooß, J.-U., Engel, I., Borrmann, S., Frey, W., Günther, G., Hoyle, C. R., Kivi, R., Luo, B. P., Molleker, S., Peter, T., Pitts, M. C., Schlager, H., Stiller, G., Vömel, H., Walker, K. A., and Müller, R.: Nitric acid trihydrate nucleation and denitrification in the Arctic stratosphere, Atmos. Chem. Phys., 14, 1055–1073, 2014.

Hanson, D. and Mauersberger, K.: Laboratory studies of the nitric acid trihydrate: Implications for the south polar stratosphere, Geophys. Res. Lett., 15, 855–858, 1988.

Hendricks, E. A., Doyle, J. D., Eckermann, S. D., Jiang, Q., and Reinecke, P. A.: What is the source of the stratospheric gravity wave belt in austral winter?, J. Atmos. Sci., 71, 1583–1592, 2014.

Hindley, N. P., Wright, C. J., Smith, N. D., and Mitchell, N. J.: The southern stratospheric gravity wave hot spot: individual waves and their momentum fluxes measured by COSMIC GPS-RO, Atmos. Chem. Phys., 15, 7797–7818, 2015.

Hitchman, M. H., Buker, M. L., Tripoli, G. J., Browell, E. V., Grant, W. B., McGee, T. J., and Burris, J. F.: Nonorographic generation of Arctic polar stratospheric clouds during December 1999, J. Geophys. Res., 108, 8325, doi:10.1029/2001JD001034, 2003.

Hoffmann, L. and Alexander, M. J.: Retrieval of stratospheric temperatures from Atmospheric Infrared Sounder radiance measurements for gravity wave studies, J. Geophys. Res., 114, D07105, doi:10.1029/2008JD011241, 2009.

5   Hoffmann, L. and Alexander, M. J.: Occurrence frequency of convective gravity waves during the North American thunderstorm season, J. Geophys. Res., 115, D20111, doi:10.1029/2010JD014401, 2010.

Hoffmann, L., Xue, X., and Alexander, M. J.: A global view of stratospheric gravity wave hotspots located with Atmospheric Infrared Sounder observations, J. Geophys. Res., 118, 416–434, 2013.

Hoffmann, L., Alexander, M. J., Clerbaux, C., Grimsdell, A. W., Meyer, C. I., Rößler, T., and Tournier, B.: Intercomparison of stratospheric
10   gravity wave observations with AIRS and IASI, Atmos. Meas. Tech., 7, 4517–4537, 2014.

Hoffmann, L., Grimsdell, A. W., and Alexander, M. J.: Stratospheric gravity waves at Southern Hemisphere orographic hotspots: 2003–2014 AIRS/Aqua observations, Atmos. Chem. Phys., 16, 9381–9397, 2016a.

Hoffmann, L., Rößler, T., Griessbach, S., Heng, Y., and Stein, O.: Lagrangian transport simulations of volcanic sulfur dioxide emissions: impact of meteorological data products, J. Geophys. Res., doi:10.1002/2015JD023749, 2016b.

15   Holton, J. R.: The role of gravity wave induced drag and diffusion on the momentum budget of the mesosphere, J. Atmos. Sci., 39, 791–799, 1982.

Höpfner, M., Larsen, N., Spang, R., Luo, B. P., Ma, J., Svendsen, S. H., Eckermann, S. D., Knudsen, B., Massoli, P., Cairo, F., Stiller, G., v. Clarmann, T., and Fischer, H.: MIPAS detects Antarctic stratospheric belt of NAT PSCs caused by mountain waves, Atmos. Chem. Phys., 6, 1221–1230, 2006a.

20   Höpfner, M., Luo, B. P., Massoli, P., Cairo, F., Spang, R., Snels, M., Di Donfrancesco, G., Stiller, G., von Clarmann, T., Fischer, H., and Biermann, U.: Spectroscopic evidence for NAT, STS, and ice in MIPAS infrared limb emission measurements of polar stratospheric clouds, Atmos. Chem. Phys., 6, 1201–1219, 2006b.

Hoyle, C. R., Engel, I., Luo, B. P., Pitts, M. C., Poole, L. R., Grooß, J.-U., and Peter, T.: Heterogeneous formation of polar stratospheric clouds – Part 1: Nucleation of nitric acid trihydrate (NAT), Atmos. Chem. Phys., 13, 9577–9595, 2013.

25   Jewtoukoff, V., Hertzog, A., Plougonven, R., Cámara, A. d. l., and Lott, F.: Comparison of Gravity Waves in the Southern Hemisphere Derived from Balloon Observations and the ECMWF Analyses, J. Atmos. Sci., 72, 3449–3468, 2015.

Kim, S., Chun, H., and Wu, D. L.: A study on stratospheric gravity waves generated by Typhoon Ewiniar: Numerical simulations and satellite observations, J. Geophys. Res., 114, D22104, doi:10.1029/2009JD011971, 2009.

Kohma, M. and Sato, K.: The effects of atmospheric waves on the amounts of polar stratospheric clouds, Atmos. Chem. Phys., 11, 11 535–
30   11 552, 2011.

Lambert, A., Santee, M. L., Wu, D. L., and Chae, J. H.: A-train CALIOP and MLS observations of early winter Antarctic polar stratospheric clouds and nitric acid in 2008, Atmos. Chem. Phys., 12, 2899–2931, 2012.

Lindzen, R. S.: Turbulence and stress due to gravity wave and tidal breakdown, J. Geophys. Res., 86, 9707–9714, 1981.

Marti, J. and Mauersberger, K.: Laboratory simulations of PSC particle formation, Geophys. Res. Lett., 20, 359–362, 1993.

35   McDonald, A. J., George, S. E., and Woollands, R. M.: Can gravity waves significantly impact PSC occurrence in the Antarctic?, Atmos. Chem. Phys., 9, 8825–8840, 2009.

McNally, A. P., Watts, P. D., A. Smith, J., Engelen, R., Kelly, G. A., Thépaut, J. N., and Matricardi, M.: The assimilation of AIRS radiance data at ECMWF, Quart. J. Roy. Meteorol. Soc., 132, 935–957, 2006.

Nastrom, G. D. and Fritts, D. C.: Sources of mesoscale variability of gravity waves. Part I: topographic excitation, J. Atmos. Sci., 49, 101–110, 1992.

National Geophysical Data Center: 2-minute Gridded Global Relief Data (ETOPO2) v2, doi:10.7289/V5J1012Q (last access: 24 November 2015), National Geophysical Data Center, NOAA, 2006.

5   Noel, V. and Pitts, M.: Gravity wave events from mesoscale simulations, compared to polar stratospheric clouds observed from spaceborne lidar over the Antarctic Peninsula, J. Geophys. Res., 117, D11207, doi:10.1029/2011JD017318, 2012.

Orr, A., Bechtold, P., Scinocca, J., Ern, M., and Janiskova, M.: Improved Middle Atmosphere Climate and Forecasts in the ECMWF Model through a Nonorographic Gravity Wave Drag Parameterization, J. Clim., 23, 5905–5926, 2010.

Orr, A., S. Hosking, J., Hoffmann, L., Keeble, J., Dean, S. M., Roscoe, H. K., Abraham, N. L., Vosper, S., and Braesicke, P.: Inclusion of

10   mountain-wave-induced cooling for the formation of PSCs over the Antarctic Peninsula in a chemistry–climate model, Atmos. Chem. Phys., 15, 1071–1086, 2015.

Pawson, S., Naujokat, B., and Labitzke, K.: On the polar stratospheric cloud formation potential of the northern stratosphere, J. Geophys. Res., 100, 23 215–23 225, 1995.

Pfister, L., Starr, W., Craig, R., Loewenstein, M., and Legg, M.: Small-Scale Motions Observed by Aircraft in the Tropical Lower Strato-

15   sphere: Evidence for Mixing and its Relationship to Large-Scale Flows, J. Atmos. Sci., 43, 3210–3225, 1986.

Pitts, M. C., Poole, L. R., and Thomason, L. W.: CALIPSO polar stratospheric cloud observations: second-generation detection algorithm and composition discrimination, Atmos. Chem. Phys., 9, 7577–7589, 2009.

Poole, L. R. and McCormick, M. P.: Airborne lidar observations of Arctic polar stratospheric clouds: Indications of two distinct growth stages, Geophys. Res. Lett., 15, 21–23, 1988.

20   Poole, L. R. and Pitts, M. C.: Polar stratospheric cloud climatology based on Stratospheric Aerosol Measurement II observations from 1978 to 1989, J. Geophys. Res., 99, 13 083–13 089, 1994.

Randel, W., Udelhofen, P., Fleming, E., Geller, M., Gelman, M., Hamilton, K., Karoly, D., Ortland, D., Pawson, S., Swinbank, R., Wu, F., Baldwin, M., Chanin, M.-L., Keckhut, P., Labitzke, K., Remsberg, E., Simmons, A., and Wu, D.: The SPARC Intercomparison of middle atmosphere climatologies, J. Clim., 17, 986–1003, 2004.

25   Sato, K., Tateno, S., Watanabe, S., and Kawatani, Y.: Gravity wave characteristics in the Southern Hemisphere revealed by a high-resolution middle-atmosphere general circulation model, J. Atmos. Sci., 69, 1378–1396, 2012.

Schroeder, S., Preusse, P., Ern, M., and Riese, M.: Gravity waves resolved in ECMWF and measured by SABER, Geophys. Res. Lett., 36, L10805, doi:10.1029/2008GL037054, 2009.

Shibata, T., Sato, K., Kobayashi, H., Yabuki, M., and Shiobara, M.: Antarctic polar stratospheric clouds under temperature per-

30   turbation by nonorographic inertia gravity waves observed by micropulse lidar at Syowa Station, J. Geophys. Res., 108, 4105, doi:10.1029/2002JD002713, 2003.

Smith, R. B.: On severe downslope winds., J. Atmos. Sci., 42, 2597–2603, 1985.

Solomon, S.: Stratospheric ozone depletion: A review of concepts and history, Rev. Geophys., 37, 275–316, 1999.

Solomon, S., Garcia, R. R., Rowland, F. S., and Wuebbles, D. J.: On the depletion of Antarctic ozone, Nature, 321, 755–758, 1986.

35   Spang, R., Remedios, J. J., and Barkley, M. P.: Colour indices for the detection and differentiation of cloud type in infra-red limb emission spectra, Adv. Space Res., 33, 1041–1047, 2004.

Spang, R., Remedios, J. J., Kramer, L. J., Poole, L. R., Fromm, M. D., Müller, M., Baumgarten, G., and Konopka, P.: Polar stratospheric cloud observations by MIPAS on ENVISAT: detection method, validation and analysis of the northern hemisphere winter 2002/2003, Atmos. Chem. Phys., 5, 679–692, 2005.

Spang, R., Arndt, K., Dudhia, A., Höpfner, M., Hoffmann, L., Hurley, J., Grainger, R. G., Griessbach, S., Poulsen, C., Remedios, J. J., Riese, M., Sembhi, H., Siddans, R., Waterfall, A., and Zehner, C.: Fast cloud parameter retrievals of MIPAS/Envisat, Atmos. Chem. Phys., 12, 7135–7164, 2012.

Spang, R., Hoffmann, L., Höpfner, M., Griessbach, S., Müller, R., Pitts, M. C., Orr, A. M. W., and Riese, M.: A multi-wavelength classification method for polar stratospheric cloud types using infrared limb spectra, Atmos. Meas. Tech., 9, 3619–3639, 2016.

Steele, H., Hamill, P., McCormick, M., and Swissler, T.: The formation of polar stratospheric clouds, J. Atmos. Sci., 40, 2055–2068, 1983.

Stephan, C. and Alexander, M. J.: Realistic simulations of atmospheric gravity waves over the continental U.S. using precipitation radar data, J. Adv. Model. Earth Sy., 7, 823–835, 2015.

Stockwell, R. G., Mansinha, L., and Lowe, R.: Localization of the complex spectrum: the S transform, IEEE Trans. Signal Process., 44, 998–1001, 1996.

Toon, O. B., Hamill, P., Turco, R. P., and Pinto, J.: Condensation of HNO_3 and HCl in the winter polar stratospheres, Geophys. Res. Lett., 13, 1284–1287, 1986.

Tsuda, T., Murayama, Y., Wiryosumarto, H., Harijono, S. W. B., and Kato, S.: Radiosonde observations of equatorial atmosphere dynamics over Indonesia. 2. Characteristics of gravity waves, J. Geophys. Res., 99, 10 507–10 516, 1994.

Winker, D. M., Pelon, J., Coakley, J. A., Ackerman, S. A., Charlson, R. J., Colarco, P. R., Flamant, P., Fu, Q., Hoff, R. M., Kittaka, C., Kubar, T. L., Le Treut, H., McCormick, M. P., Mégie, G., Poole, L., Powell, K., Trepte, C., Vaughan, M. A., and Wielicki, B. A.: The CALIPSO Mission: A Global 3D View of Aerosols and Clouds, B. Am. Meteorol. Soc., 91, 1211–1229, 2010.

Worsnop, D. R., Zahniser, M. S., Fox, L. E., and Wofsy, S. C.: Vapor pressures of solid hydrates of nitric acid: Implications for polar stratospheric clouds, Science, 259, 71–74, 1993.

Wu, D. L.: Mesoscale gravity wave variances from AMSU-A radiances, Geophys. Res. Lett., 31, L12114, doi:10.1029/2004GL019562, 2004.

Wu, D. L. and Eckermann, S. D.: Global gravity wave variances from Aura MLS: characteristics and interpretation, J. Atmos. Sci., 65, 3695–3718, 2008.

Wu, D. L. and Jiang, J. H.: MLS observations of atmospheric gravity waves over Antarctica, J. Geophys. Res., 107, 4773, doi:10.1029/2002JD002390, 2002.

Wu, D. L. and Zhang, F.: A study of mesoscale gravity waves over the North Atlantic with satellite observations and a mesoscale model, J. Geophys. Res., 109, D22104, doi:10.1029/2004JD005090, 2004.

Wu, J. F., Xue, X. H., Hoffmann, L., Dou, X. K., Li, H. M., and Chen, T. D.: A case study of typhoon-induced gravity waves and the orographic impacts related to Typhoon Mindulle (2004) over Taiwan, J. Geophys. Res., 120, 9193–9207, 2015.

Zhang, R., Wooldridge, P. J., and Molina, M. J.: Vapor pressure measurements for the $H_2SO_4/HNO_3/H_2O$ and $H_2SO_4/HCl/H_2O$ systems: Incorporation of stratospheric acids into background sulfate aerosols, J. Phys. Chem., 97, 8541–8548, 1993.

Table 1. AIRS Radiance Channels of the 15 μm Brightness Temperature Data Product

Channel Number	Wave-number [cm^{-1}]	NEdT at 250 K [K]	Channel Number	Wave-number [cm^{-1}]	NEdT at 250 K [K]
5	650.6	0.60	101	674.4	0.42
11	652.0	0.67	102	674.7	0.44
17	653.5	0.61	107	676.0	0.45
23	654.9	0.61	108	676.2	0.42
30	656.6	0.54	113	677.5	0.39
36	658.1	0.51	114	677.8	0.43
42	659.6	0.47	119	679.1	0.42
56	663.0	0.46	120	679.4	0.45
84	670.1	0.49	125	680.7	0.41
89	671.3	0.39	126	680.9	0.41
95	672.9	0.43			

Table 2. Northern Hemisphere Gravity Wave-induced PSC Formation Events

Date	Source Region	Date	Source Region
2003-02-10	Ural Mountains	2008-01-01	Iceland
2005-01-27	Scandinavian Mountains	2008-01-28	Iceland
2005-02-16	Greenland	2008-02-10	Iceland
2005-02-18	Greenland	2008-12-24	Iceland
2006-01-19	United Kingdom	2010-01-03	Greenland
2006-12-26	Scandinavian Mountains	2010-12-07	Greenland
2007-01-25	Greenland	2011-01-06	non-orographic
2007-02-13	Labrador	2011-01-29	East Siberian Plateau
2007-12-21	Scandinavian Mountains	2011-12-27	Scandinavian Mountains
		2011-12-29	United Kingdom

Table 3. Southern Hemisphere Gravity Wave-induced PSC Formation Events

Date	Source Region	Date	Source Region
2003-06-11	Antarctic Peninsula	2009-06-02	Mac Robertson Land
2003-06-30	Antarctic Peninsula	2009-06-27	Antarctic Peninsula
2003-08-23	Transantarctic Mountains	2009-07-19	Antarctic Peninsula
2003-09-10	Antarctic Peninsula	2009-07-24	non-orographic
2003-09-16	Antarctic Peninsula	2009-09-10	Transantarctic Mountains
2005-06-08	Marie Byrd Land	2010-06-11	Antarctic Peninsula
2005-06-14	Antarctic Peninsula	2010-07-21	Antarctic Peninsula
2006-06-28	Antarctic Peninsula	2010-07-30	Marie Byrd Land
2007-07-08	Antarctic Peninsula	2010-08-16	Antarctic Peninsula
2007-08-04	Transantarctic Mountains	2011-06-24	Enderby Land
2007-08-16	Antarctic Peninsula	2011-06-26	Antarctic Peninsula
2007-09-10	Antarctic Peninsula	2011-08-05	Antarctic Peninsula
2008-05-29	Antarctic Peninsula		
2008-07-25	Transantarctic Mountains		
2008-08-29	Mac Robertson Land		
2008-09-12	Antarctic Peninsula		
2008-09-22	Antarctic Peninsula		

Table 4. Estimation of Gravity Wave Amplitudes for the Orographic Events Shown in Fig. 11

Event Date	u	λ_x	λ_z	R	BT'	T'
	$[\mathrm{m\,s^{-1}}]$	[km]	[km]	[%]	[K]	[K]
2007-01-25	65	113	20.7	21.6	1.8	8.3
2007-07-08	55	111	17.5	15.4	1.4	9.1
2008-07-25	65	128	20.7	21.6	2.6	12.0
2008-08-29	60	95	19.2	18.5	1.3	7.0
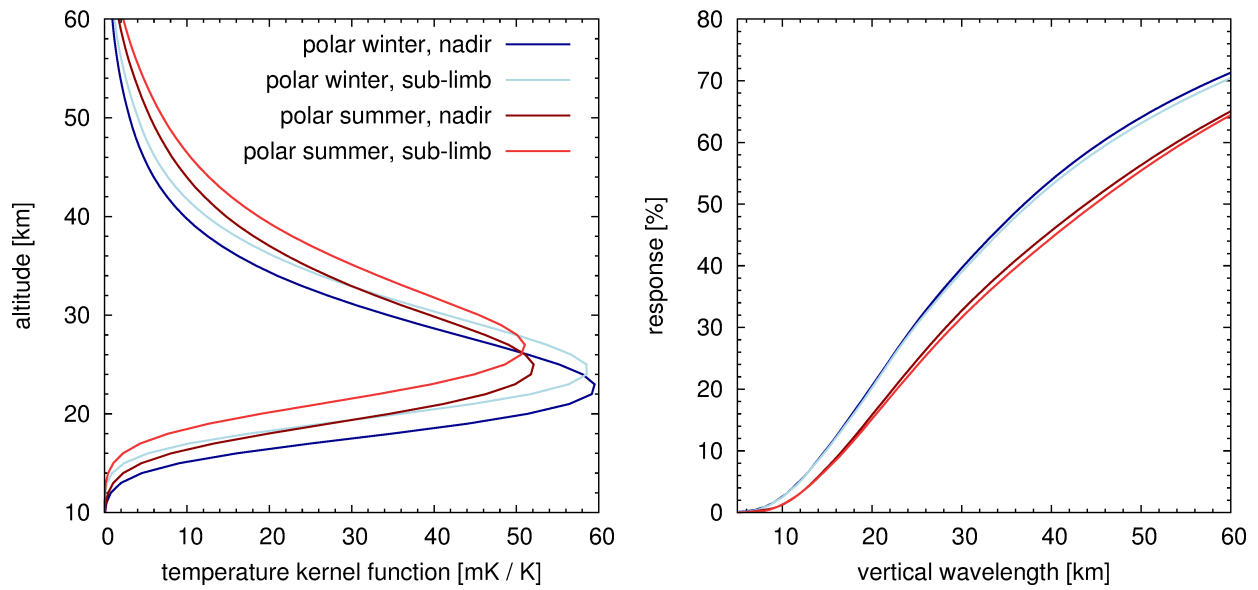
Figure 1. Temperature weighting functions (left) and amplitude response curves (right) for the AIRS 15 μm brightness temperature data set. Radiative transfer calculations have been performed for polar summer and polar winter conditions, the nadir direction and the outermost scan angles (referred to as 'sub-limb'), and a 1 km altitude grid.
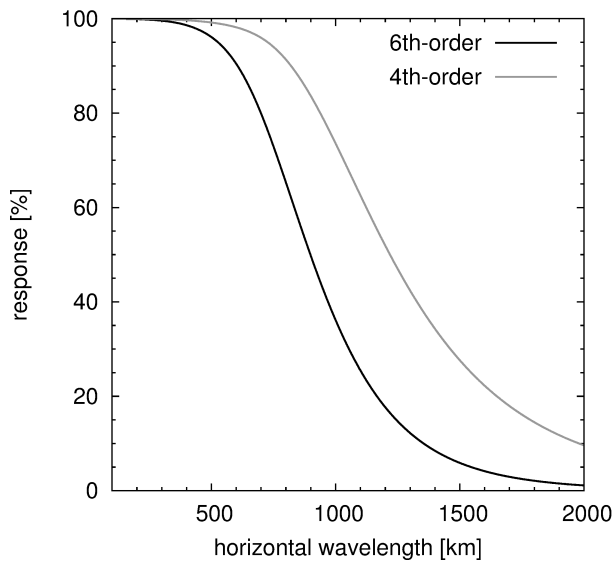
Figure 2. Amplitude response of the AIRS 15 μm brightness temperature data set for gravity waves with different across-track wavelengths. The plot shows the response using a 4th- or 6th-order polynomial fit to estimate background signals.
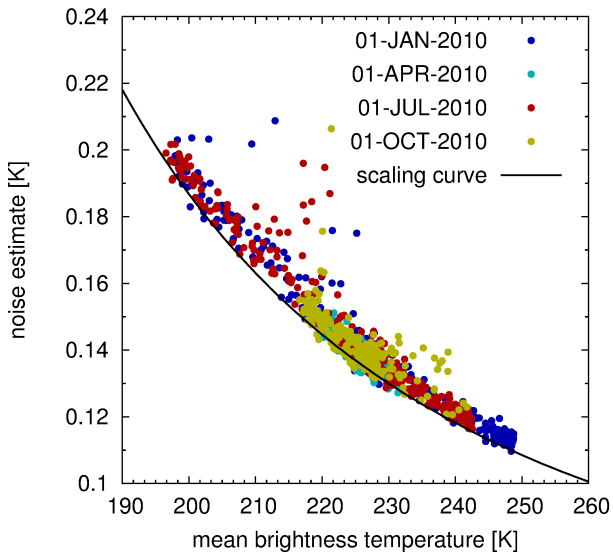
Figure 3. Noise estimates for the AIRS 15 μm brightness temperature data set versus mean background temperature. Individual noise estimates (colored dots) have been obtained from radiance measurements within globally distributed boxes of 90×90 satellite footprints on different days. Few outliers with high noise are due to cases with small-scale waves being miss-interpreted as noise. The Planck scaling curve (black curve) is defined by a NEdT of 0.109 K at 250 K scene temperature.
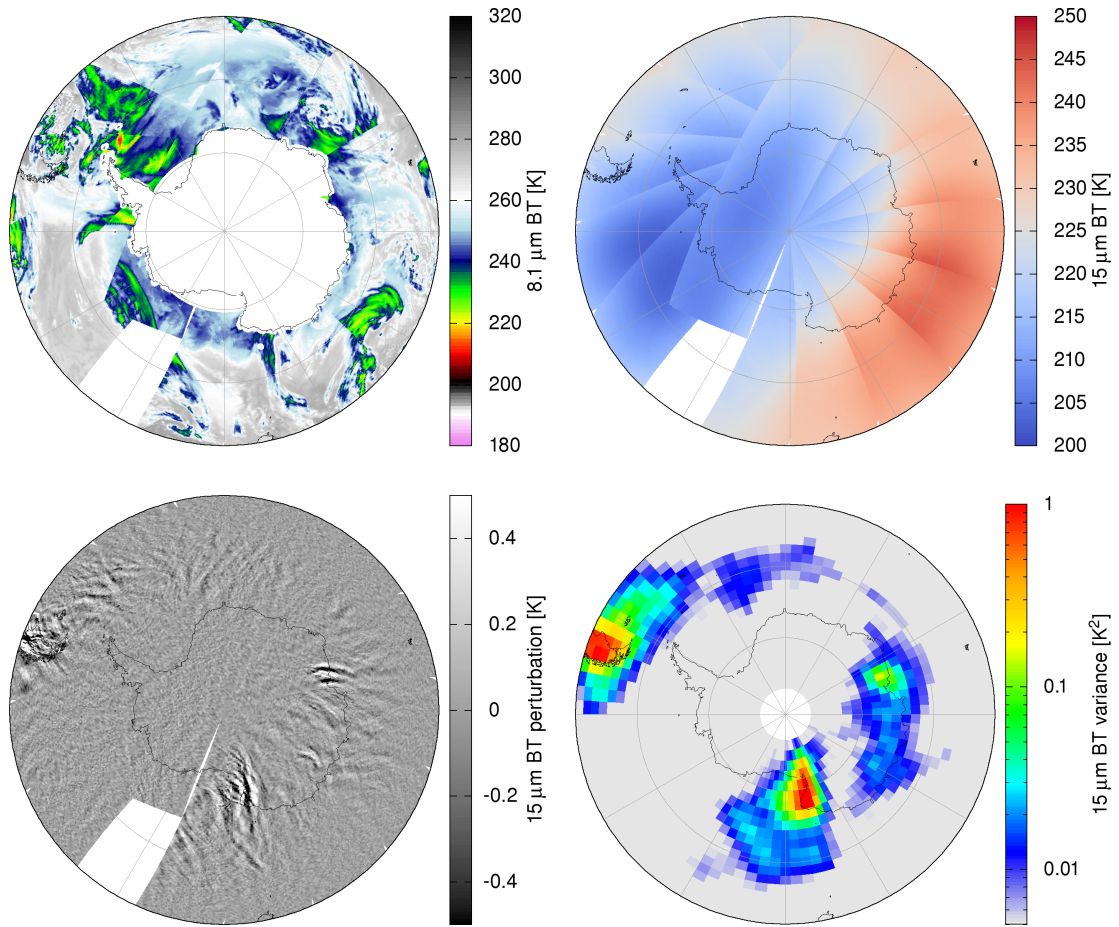
Figure 4. AIRS measurements of 8.1 μm (top, left) and 15 μm (top, right) brightness temperatures (BTs) on 24 August 2004, 12 – 24 UTC. The 8.1 μm BT observations show high clouds and storm systems. The 15 μm BT perturbation map (bottom, left) provides information on gravity waves in the lower stratosphere. BT variances on a $4° \times 2°$ horizontal grid (bottom, right) are calculated by combining measurements from 00 – 12 UTC (not shown) and 12 – 24 UTC on the given day to close data gaps and to homogenize temporal coverage.
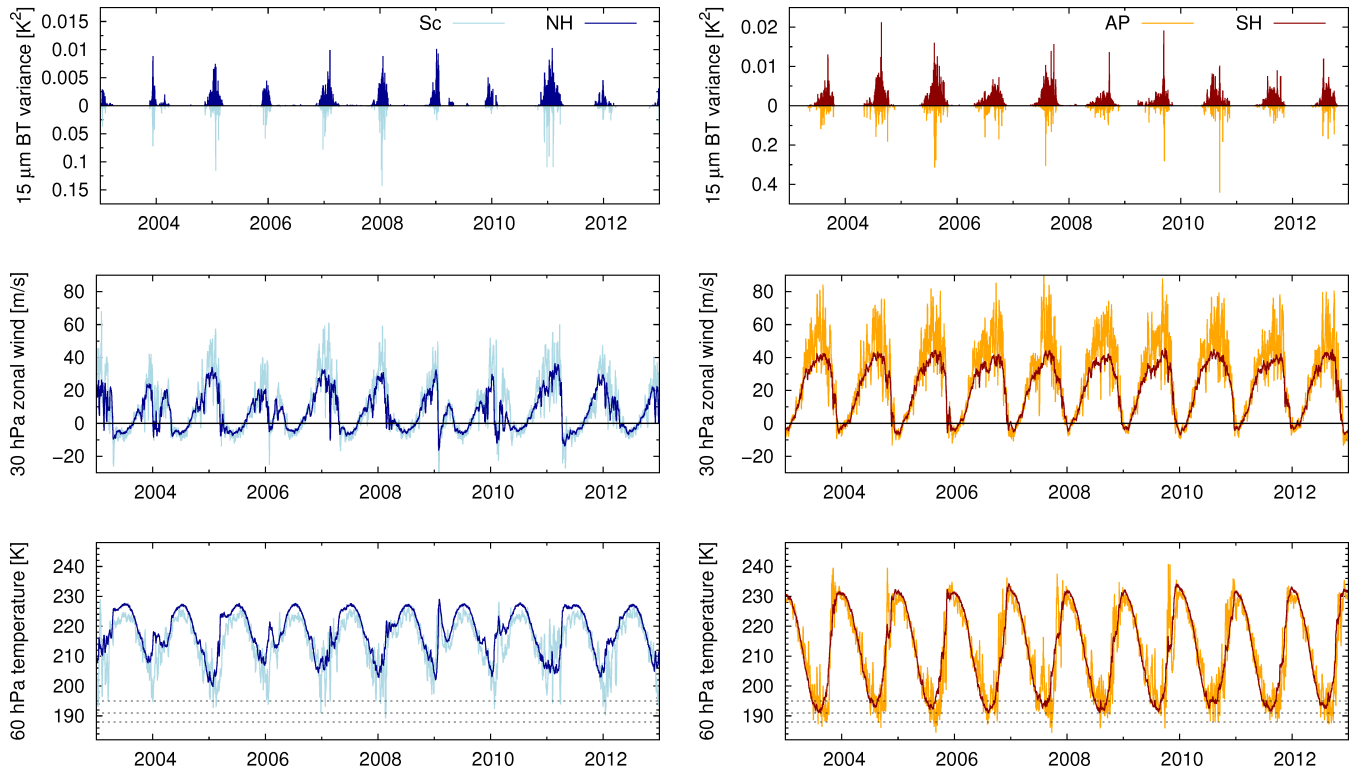
Figure 5. Time series of daily AIRS 15 μm brightness temperature variances (top) as well as 6-hourly ERA-Interim 30 hPa zonal winds (middle) and 60 hPa temperatures (bottom) at northern hemisphere mid and high latitudes (NH; 55°N – 85°N), the Scandinavian Mountains (Sc; 56°N – 64°N and 4°E – 20°E), southern hemisphere mid and high latitudes (SH; 85°S – 55°S), and the Antarctic Peninsula (AP; 68°S – 60°S and 68°W – 52°W). Dotted lines indicate typical PSC existence temperatures of $T_{ice} = 188$ K, $T_{STS} = 191$ K, and $T_{NAT} = 195$ K at 20 km altitude (Pawson et al., 1995).
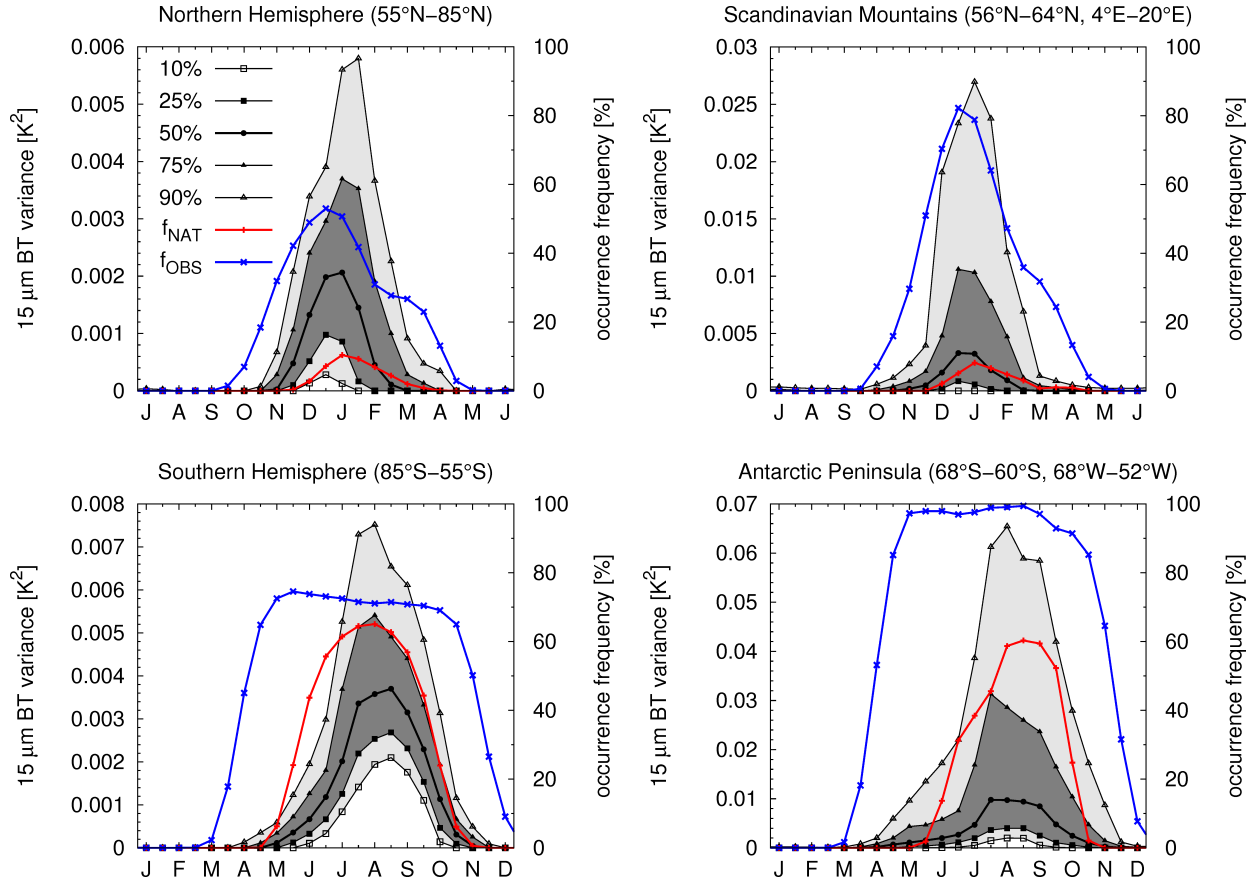
Figure 6. Seasonal cycle of gravity wave activity at northern (top, left) and southern (bottom, left) mid and high latitudes as well as the Scandinavian Mountains (top, right) and the Antarctic Peninsula (bottom, right) from AIRS observations in 2003 – 2012. Gravity wave activity within 30-day time windows is measured in terms of 10, 25, 50, 75, and 90% quantiles of 15 μm brightness temperature variances. Red curves show occurrence frequencies f_{NAT} of ERA-Interim 60 hPa temperatures falling below T_{NAT}. Blue curves show occurrence frequencies f_{OBS} of 30 hPa zonal winds exceeding a threshold of 20 m/s. Please note different scales on y-axes.
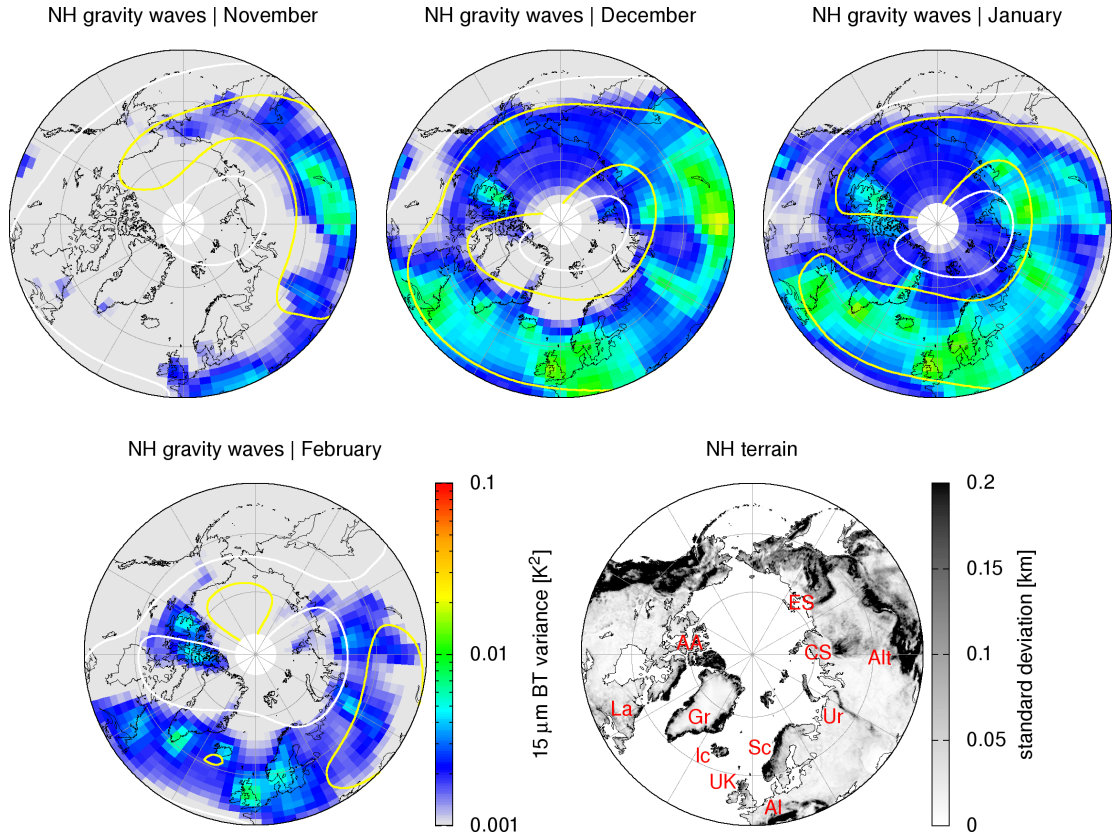
Figure 7. AIRS 2003 – 2012 monthly mean 15 μm brightness temperature variances from November to March in the northern hemisphere. Contour lines show 30 hPa ERA-Interim zonal winds at levels of 10 m s^{-1} (white), 20 m s^{-1} (yellow), 40 m s^{-1} (orange), and 60 m s^{-1} (red). Terrain height standard deviations on a 0.25° × 0.25° horizontal grid (bottom, right) indicate source regions of mountain waves. Red labels in the terrain map indicate the locations of the Arctic Archipelago (AA), Labrador (La), Greenland (Gr), Iceland (Ic), the United Kingdom (UK), the Scandinavian Mountains (Sc), the Alps (Al), the Ural Mountains (Ur), the Altai Mountains (Alt), the Central Siberian Plateau (CS), and the East Siberian Plateau (ES).
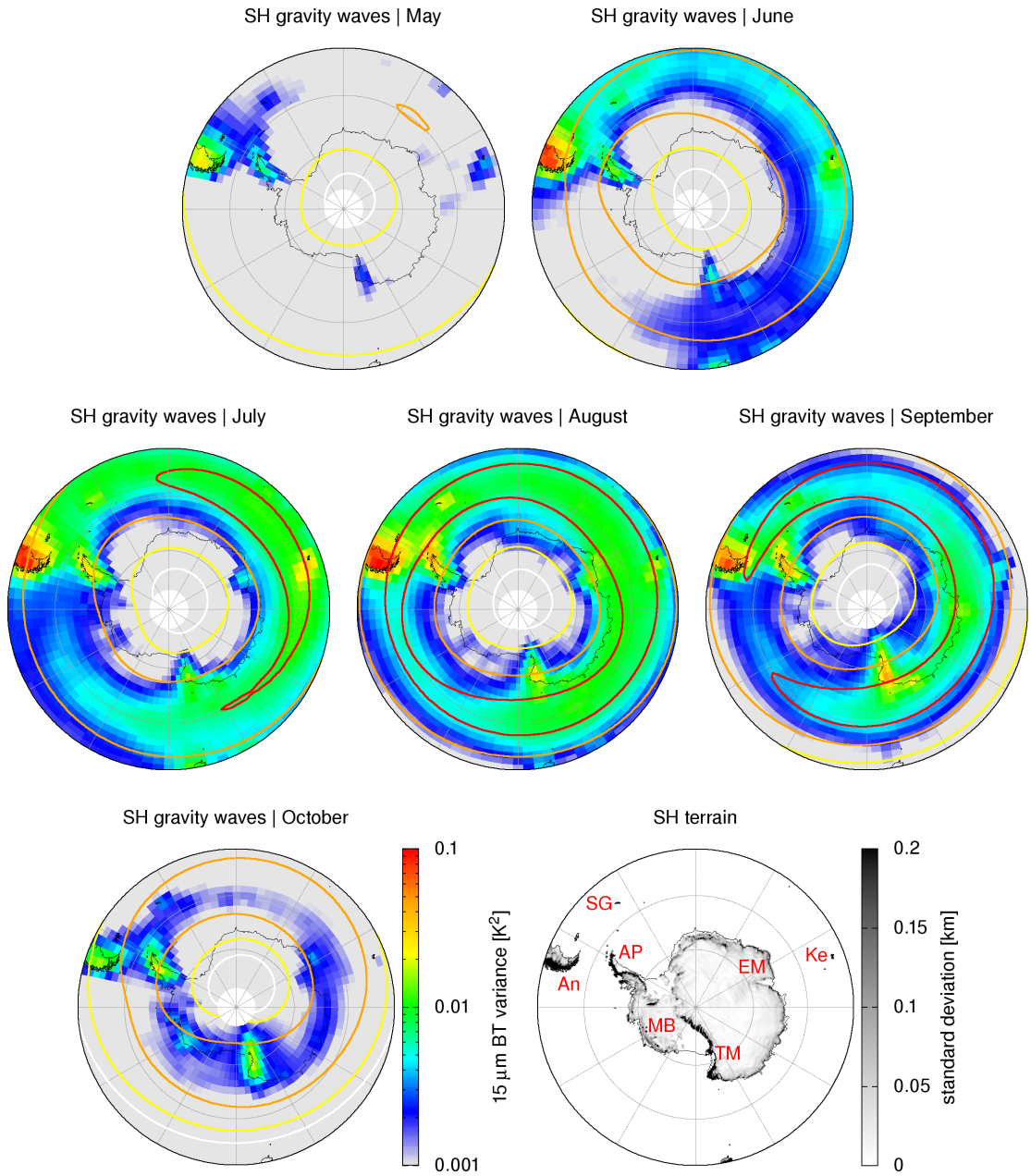
Figure 8. Same as Fig. 7, but for the southern hemisphere and the months from May to October. Red labels in the terrain map indicate the locations of Marie Byrd Land (MB), the Andes (An), the Antarctic Peninsula (AP), South Georgia (SG), Enderby Land and Mac Robertson Land (EM), the Kerguelen Islands (Ke), and the Transantarctic Mountains (TM).
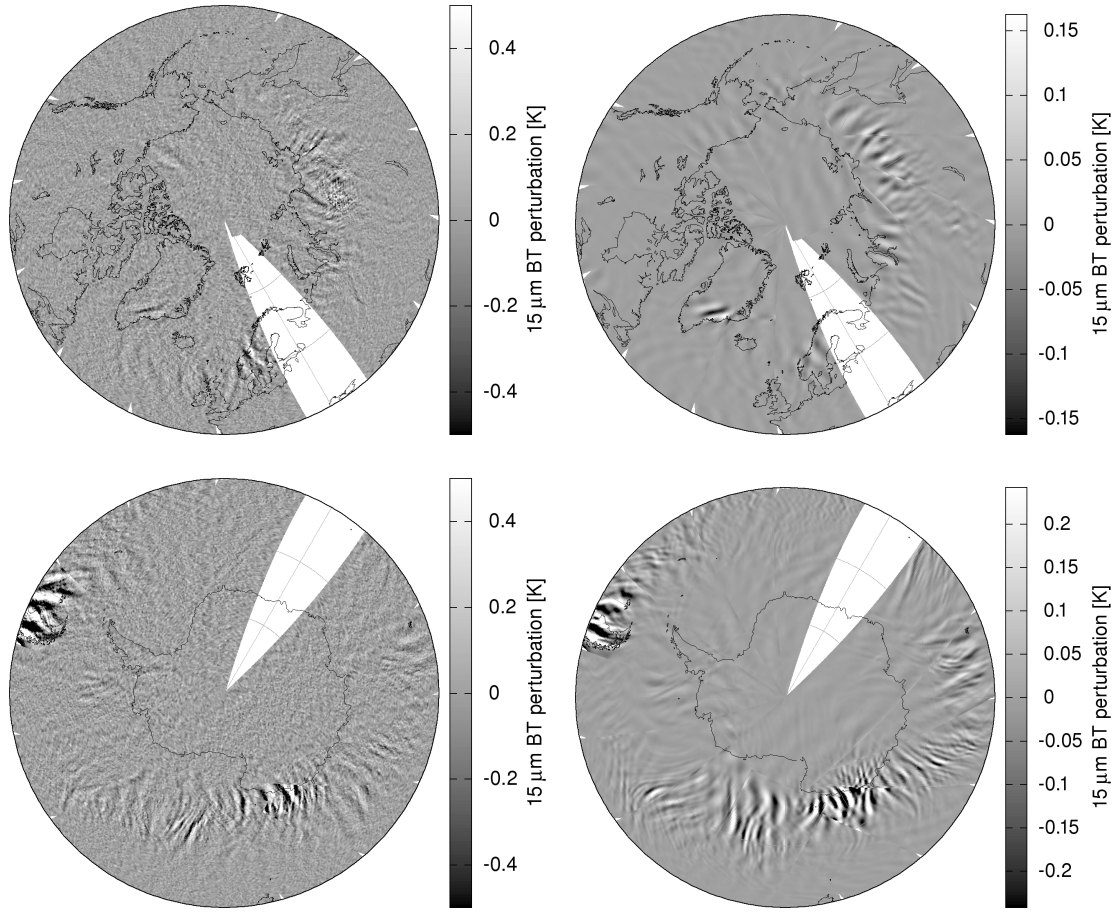
Figure 9. AIRS measurements of 15 μm brightness temperature perturbations (left) and corresponding simulations based on ECMWF operational analysis temperatures (right). Real measurements took place on 11 December 2003, 12:00 – 24:00 UTC in the northern hemisphere (top) and 22 July 2011, 00:00 – 12:00 UTC in the southern hemisphere (bottom). Simulated measurements are based on synoptic data at 18:00 and 06:00 UTC, respectively. Color bar ranges are scaled individually for better comparisons of the wave patterns.
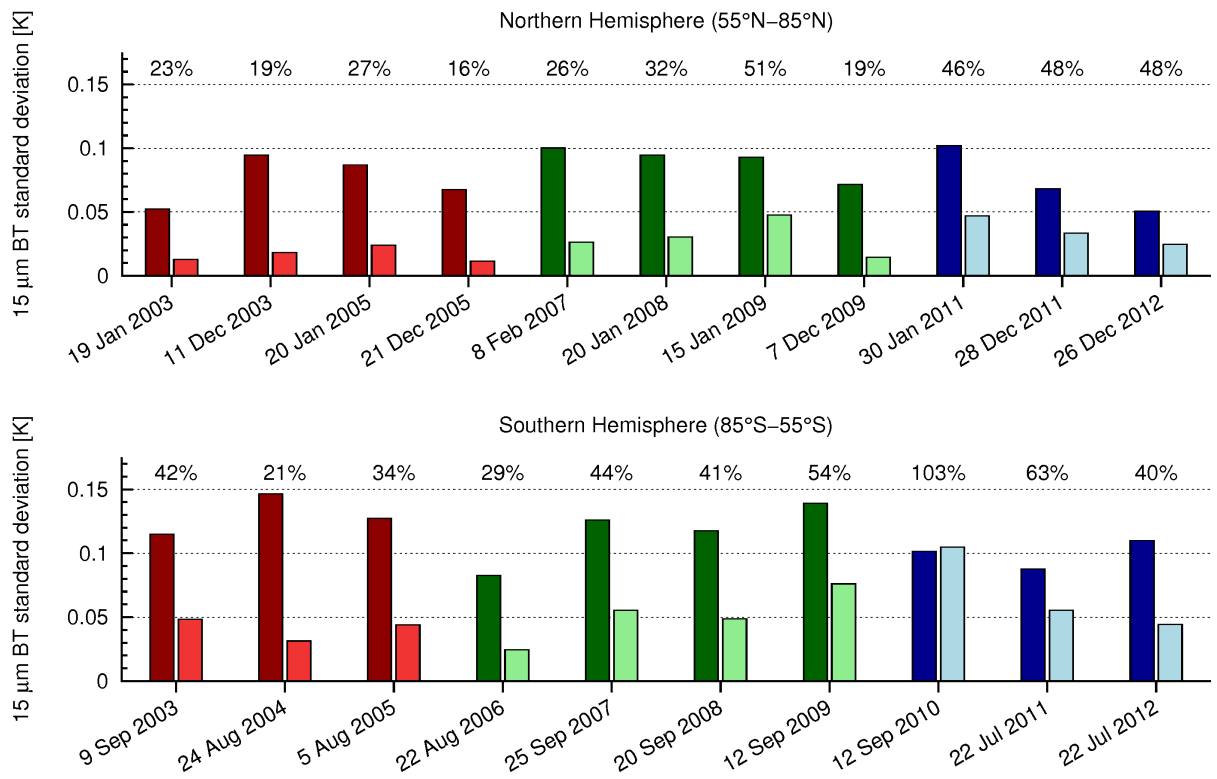
Figure 10. Peak events of gravity wave activity in individual $2003-2012$ northern and southern hemisphere winter seasons. The $15\,\mu m$ brightness temperature standard deviations were inferred from real AIRS measurements (dark shading) or simulations based on ECMWF operational analysis data (light shading). Color coding refers to the resolution of the ECMWF data (red: T511L60, green: T799L91, blue: T1279L91). Percentage numbers at the top of the plots indicate the relative differences of the simulated data with respect to the measurements.
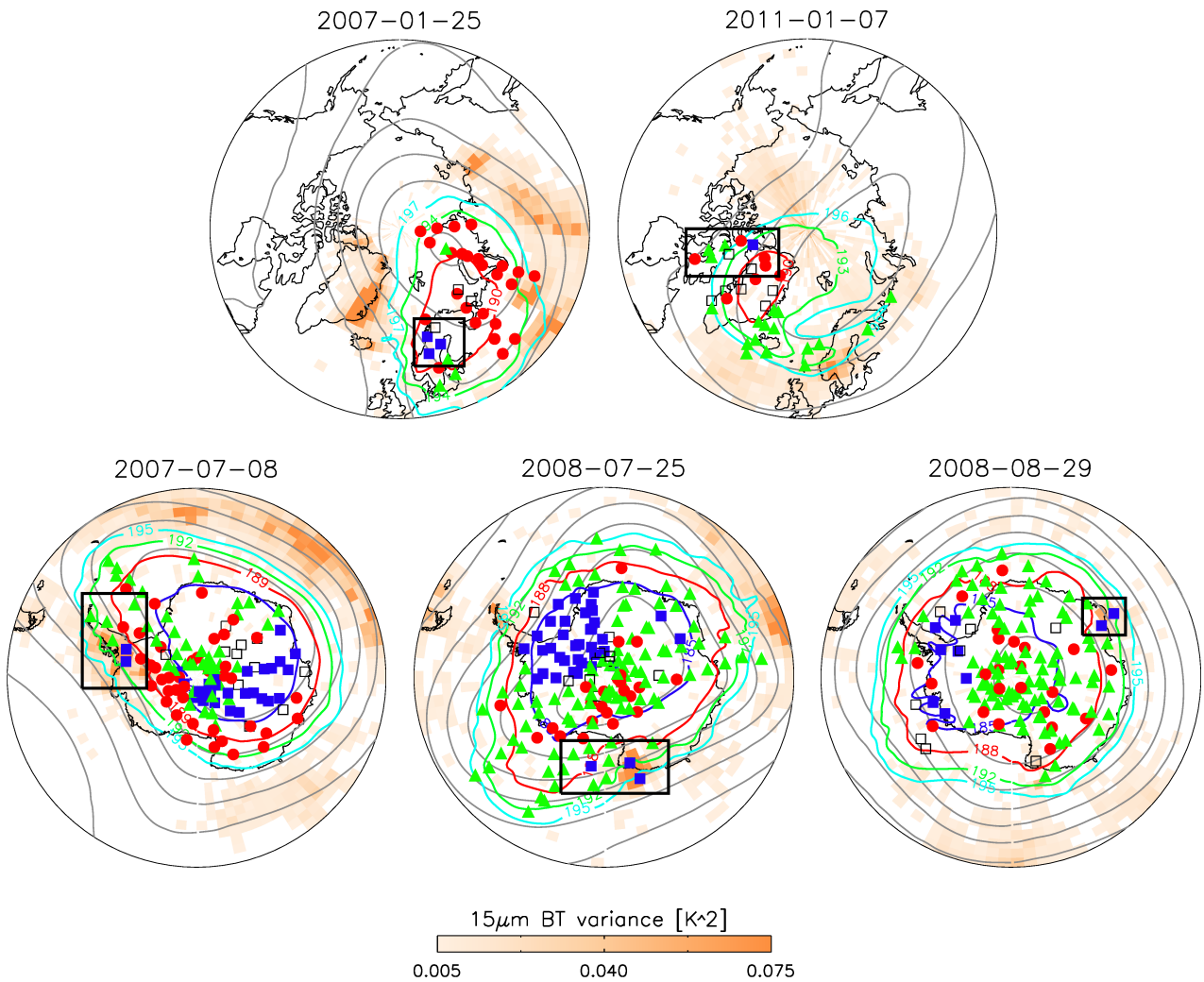
Figure 11. Examples of gravity wave-induced PSC formation events in the northern hemisphere (top) and southern hemisphere (bottom). Events are indicated by black boxes. The orange shading shows detrended and noise-corrected AIRS 15 μm brightness temperature variances. Symbols show MIPAS PSC observations (ice: blue squares, STS: red circles, NAT: green triangles, unclassified: black squares) at $450-550$ K potential temperature. Contour lines indicate PSC existence temperatures (T_{ice}: blue, T_{STS}: red, T_{NAT}: green, $T_{NAT}+3$ K: cyan) and the Montgomery stream function (gray) at the 500 K isentropic level.
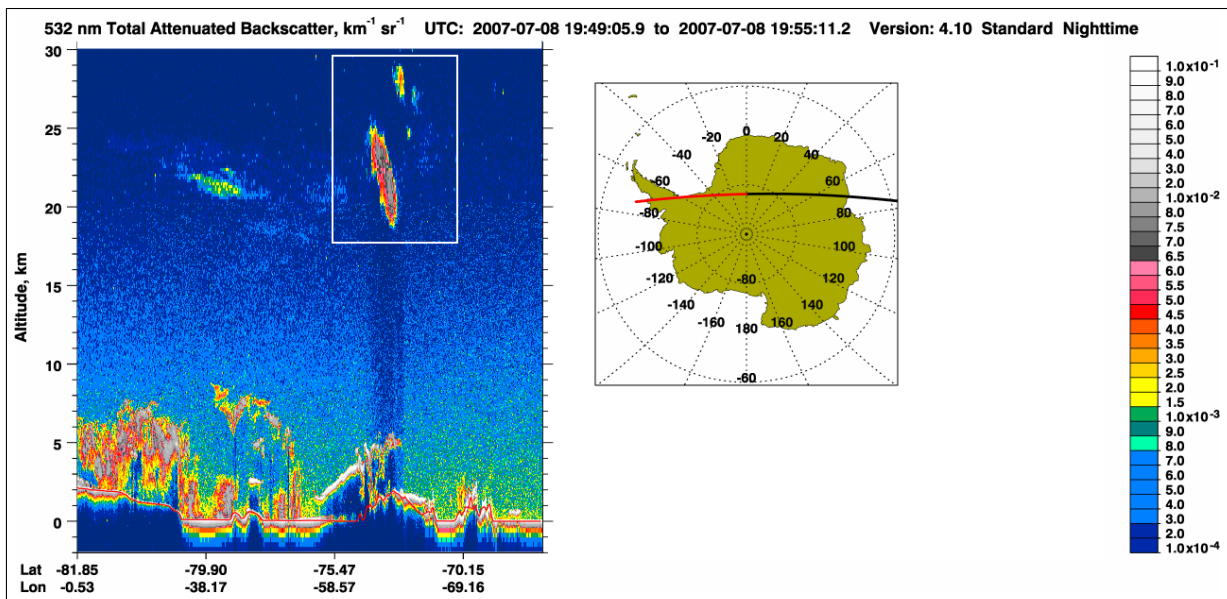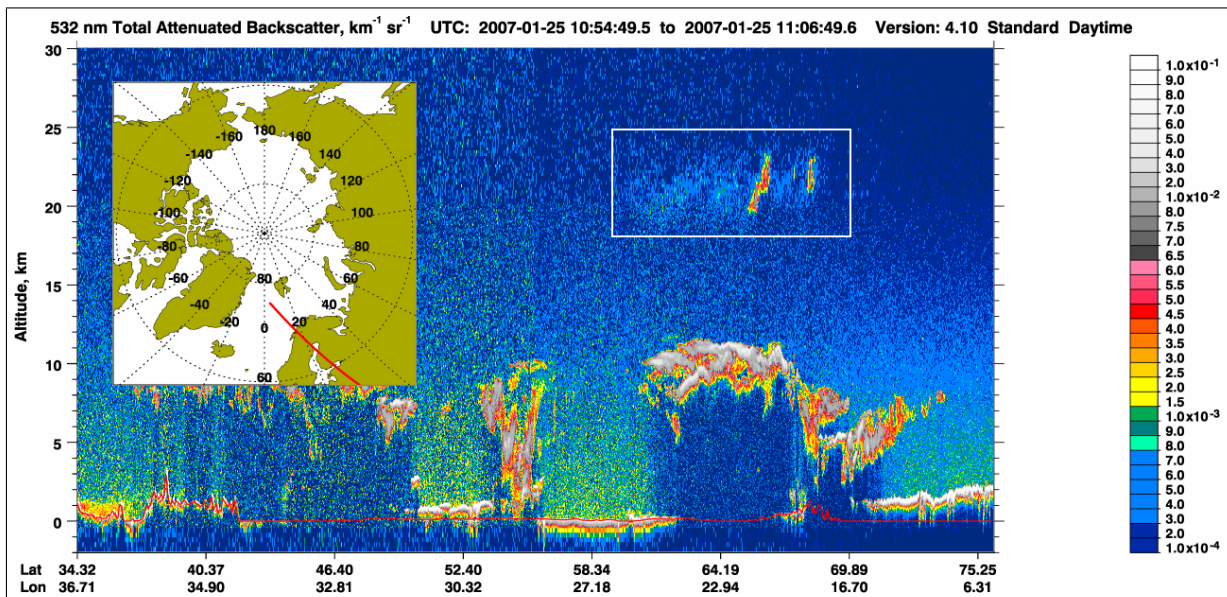
Figure 12. CALIOP browse images of 532 nm total attenuated backscatter for two of the case studies presented in Fig. 11. Inset maps show the satellite track. White boxes indicate features associated with polar stratospheric clouds.
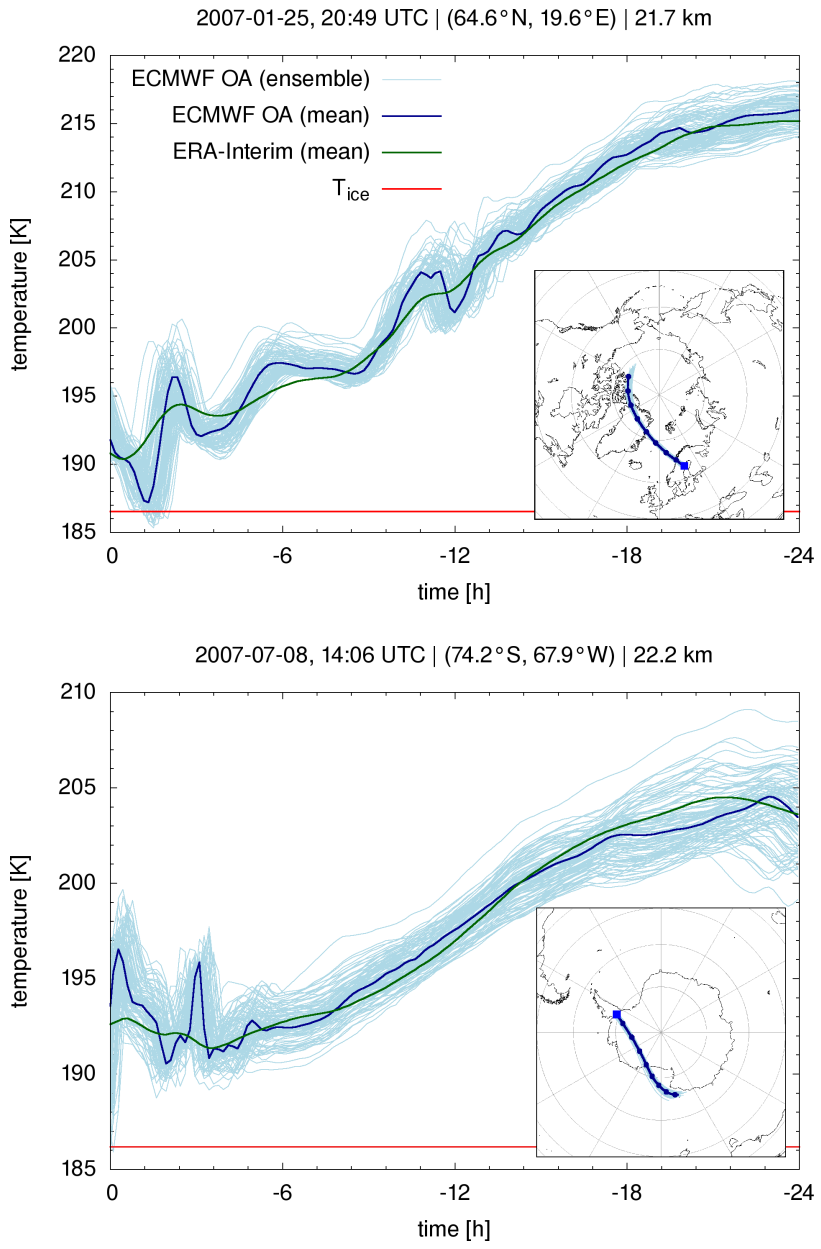
Figure 13. Temperature time series from backward trajectory calculations for two of the case studies presented in Fig. 11. See plot titles for time and location of MIPAS detections of ice PSCs that are used to define the trajectory seeds. Note that the time is displayed on a reversed x-axis, with the MIPAS detection being located at 0 h. Calculations are based on ERA-Interim (green) and ECMWF operational analysis (OA; blue) meteorological data. Inset maps show the trajectory paths.